



A multi-objective optimization design of industrial robot arms



Sallam A. Kouritem ^{a,*}, Mohammed I. Abouheaf ^{b,*}, Nabil Nahas ^c,
Mohamed Hassan ^a

^a Department of Mechanical Engineering, Faculty of Engineering, Alexandria University, Alexandria 21544, Egypt

^b College of Technology, Architecture & Applied Engineering, Bowling Green State University, Bowling Green, 43402 OH, USA

^c Faculté d'administration, Université de Moncton, Moncton, E1A 3E9 NB, Canada

Received 9 February 2022; revised 7 June 2022; accepted 26 June 2022

Available online 8 July 2022

KEYWORDS

Stress analysis;
Vibration analysis;
Finite element method;
Kinematics;
Self-adjusting optimization

Abstract This paper introduces a multi-objective design mechanism to minimize both the initial and running costs of industrial robot arms. The goal of the design problem is to decide the type of material and physical dimensions of the robot arm to withstand high loads at vulnerable locations using stress analysis. Additionally, it selects the material architecture for the robot links based on a vibration analysis to avoid robot failure at or close to the resonance frequency. Hence, a set of design equations based on stress analysis are developed using analytical approaches while the findings are supported by finite element simulations in ANSYS. These decide the type of material, cross-section area, factor of safety (FoS), and maximum deflection of the robot links in terms of the mass-loads. Moreover, the vibration analysis is conducted to enhance the dynamic characteristics of the robot arm. Therefore, the excitation frequency is modified by changing the mass and the robot segment-material to evade working at the natural frequency. Modal analysis is conducted using ANSYS to identify the fundamental frequencies and their modal shapes. Then, a material selection mechanism based on finite element analysis is considered to allow a safe frequency operation range for the robot arm. A customized robot arm structure that combines Magnesium and Aluminum alloy with highly improved FoS and minimizes the initial and operating costs is proposed. In addition to the body structure of the robot arm, the influence of the reducers and motors on the stiffness and vibration of the robot arm is presented. Finally, the motion of the robot arm is optimized using a Genetic Algorithm subject to a set of boundary conditions imposed by the desired mission. The effect of rotation angle value in the power consumption is presented. The coefficients of a developed angular displacement function are optimized to ensure minimum power consumption during the robot missions.

© 2022 THE AUTHORS. Published by Elsevier BV on behalf of Faculty of Engineering, Alexandria University. This is an open access article under the CC BY-NC-ND license (<http://creativecommons.org/licenses/by-nc-nd/4.0/>).

* Corresponding authors.

E-mail addresses: sallam.kouritem@alexu.edu.eg (S.A. Kouritem), mabouhe@bgsu.edu (M.I. Abouheaf), nabil.nahas@umanitoba.ca (N. Nahas), mm.hassan@alexu.edu.eg (M. Hassan).

Peer review under responsibility of Faculty of Engineering, Alexandria University.

1. Introduction

The modeling, design, and control aspects of robotic systems have attracted increasing attention during the last three decades [1–5]. Such systems have been used in different applications ranging from domestic to industrial ones [6–10]. Intuitive modeling approaches have been employed to discuss the robotic topology, in terms of motion and structure. The design of the connection links and distribution of joints, for instance, rely on the proper selection of physical as well as architectural parameters such as material, dimensions, mass/inertia, etc [11–13]. Further, the optimization of robot performance relies on analyzing the robot's dynamics and kinematics. This is done to minimize certain utility functions that reflect the optimization objectives. The Denavit–Hartenberg (DH) parameters explain the kinematic chains for robotic manipulators up to 6 Degrees of Freedom (DoF), through attaching reference frames to the links [14]. In some cases, the DH parameters are utilized to optimize the kinematic path [15–18]. The SCARA robot arm is modeled and simulated as a Prismatic Rotation Rotation (PRR) type manipulator, where the forward, inverse kinematics, and DH parameters are employed to evaluate the link lengths of this robotic arm [19].

Many optimization approaches have been developed for industrial robots to maximize efficiency, customize geometric layouts, and enhance performance. The Genetic Algorithm (GA) was employed to optimize the robotic systems in different aspects such as optimizing the path-following task of mobile robots [20], deciding suitable torques to minimize the trajectory-tracking errors in 6 DoF robots [21], minimizing the vibration and life cycle-time of 6 DoF robot arm [22], and customizing the geometry and topology of robotic systems [23]. Other optimization techniques have been employed to support the stress and vibration analysis of the different robotic systems. The static stress analysis and strength tests are used to advise the material of the robot links and hence address the deformation issues subject to different load capacities [24]. The Finite Element Method (FEM) has been employed to understand the distributions of maximum applicable stresses and deformations of 6 DoF robotic arms to better stabilize the robot [25]. Several approaches are considered to optimize the performance of robotic systems by providing geometric and structural solutions [26–29]. These approaches customize the robot design to increase the load-carrying capacity [30], do vibration analysis studies for Aristo robots to avoid

resonance [31], and reconfigure the robot material structure to adjust the weights [32]. Many optimization techniques were conducted for power systems optimization applications using iterative(systematic) optimization techniques [33–37].

The contributions of this study are three-fold; First, the work introduces a design mechanism to restructure the robot arm according to analytical as well as FEM simulations in ANSYS. The stress analysis is employed to decide the material of the robot arm to withstand different load capacities. Further, the Factor of Safety (FoS) and the deformation values of five types of material are assessed analytically and numerically as well using Finite Element Analysis (FEA). These are expressed as functions of the cross-section areas and the mass loads to enable flexibility in the design. Second, the vibration analysis is conducted where the FEA is used to evaluate the natural frequencies and mode shapes using ANSYS, as inspired by [38]. Moreover, the structure of the robot arm is re-configured to avoid the resonance frequencies by considering combinations of material. Finally, GA is employed to minimize the consumed power by the motors due to the motion of the robot arm, where the angular velocities and torques of the joints are minimized. Fig. 1 summarizes the design optimization procedures of the studied robot arm used in this paper.

The paper is organized as follows; Section 2 briefly introduces the methodologies and software engines used in this work. The stress analysis is conducted using an analytical approach and FEA simulations as well in Section 3. Section 4 shows the material restructuring of the robot arm according to the vibration analysis. The GA optimization approach is employed to provide efficient power and motion schemes for the robot arm made of Alliuminium-Alloy in Section 5. Then, the Robo-Analyzer software is employed to customize a set of alternative solutions for a robot mission. Finally, some concluding remarks are presented in Section 7.

2. Modelling and methodology

This section highlights the methodologies and simulation tools used in the work. The study is conducted on a 6 DoF robot arm that involves a base twist, two-rotational axes (2, 3), and 3 DoF gripper (d_4, d_5, d_6) to ensure flexible end effector operation, as shown by Fig. 2. The offset of joint i (d_i), refers to the motor installation position and θ_i indicates the rotation angle of each joint i . The dimensions and physical parameters of the robot arm are listed in Table 1. First, the robot arm is

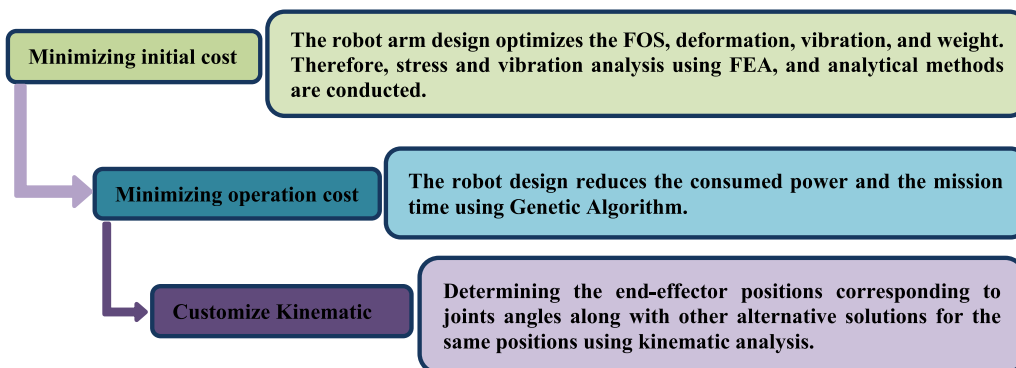


Fig. 1 Optimization procedure of the robot arm.

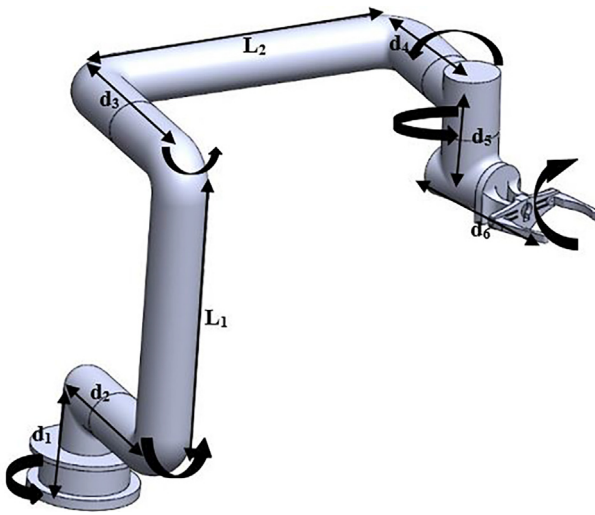


Fig. 2 3D model of the 6-DOF robot arm with its parameters.

modeled using SolidWorks and then FEM is employed to analyze and simulate the stresses using the ANSYS software engine. This allows allocating different materials to the links of the robot arm to better handle the distributions of stresses. Secondly, the vibration analysis is conducted using FEA (ANSYS) to study the mode shapes of the different frequencies of the robot arm and hence manipulate the overall frequency shapes to avoid resonance frequencies. Thirdly, the GA is considered to optimize the performance of the robot arm following a certain mission. This is done using a cost function that penalizes the sum of power consumption of the robot arm links. Finally, the Robo-Analyzer software was employed to show the forward and inverse kinematics to test the maneuverability of the outcomes.

3. Stress analysis

This section introduces a stress analysis using an analytical approach that is based on a set of approximate design equations for the robotic arm. Then, FEM is employed to investigate the stresses applied to the links of the robotic arm using ANSYS software engine. The goal is to decide a set of design factors such as material and cross-section areas, or equivalently outside diameters, to ensure a reliable operation and a cost-effective robotic arm model. This is done while satisfying certain FOS constraints of the robot arm.

3.1. Analytical stress analysis

In the sequel, the analytical foundation for the stress modeling and analysis is introduced where the simulations are conducted

using MATLAB. The robot arm is set to take the configuration shown by Fig. 3 with zero-joint angles for joints 2 and 3. This position represents the worst scenario of maximum stresses acting on the robot links. Further, it allows the study of the underlying maximum moments and bending stresses. The distributions of applied forces on the robotic arm are shown in Fig. 3(a); F_1 is a collective force representing the load-carrying capacities by the end effector, gripper weight, and gripper motor weights. The weights of the second and third axes are given the force values F_4 and F_2 , respectively. These forces are computed from the weight values and rely on the density of the selected material. Finally, F_5 and F_3 are the motor's weights at the second and third axes offset joints d_2 and d_3 (set to be 26 N each). The stress analysis study considers different types of material as reported in Table 2. The utilized materials for industrial robots depend on the specific application, density, strength, and cost. The strength/weight, cost, and the application environment are the main considerations in material selection so the Structural Steel, Aluminum alloy,[39]. Copper is suggested for its high strength and PVC is used for low weight. The advantages of the magnesium alloy of low weight, low price and low density per strength that make it attractive for many applications [40] motivate us to compare it with other materials.

The stress analysis of the robot arm is performed for hollow cross-section configurations. The outer diameter d_o exceeds the inner one d_i by 2 mm. All forces are mapped to a fixed end in terms of the moments. The maximum moments in the x and y-directions at the fixed end of the robot (i.e., second axis) are given by.

$$M_x = 700F_1 + 525F_2 + 350F_3 + 150F_4 \quad (1)$$

$$M_y = (d_2 + d_6)F_1 + d_2F_4 + (d_3 - d_2) \times F_2 + 0.5d_3(F_5 + F_3). \quad (2)$$

Hence, the total bending moment is expressed so that.

$$M_T = \sqrt{M_x^2 + M_y^2}. \quad (3)$$

The bending stress due to moment can be expressed as:

$$\sigma = \frac{M_T Y}{I} + \frac{F_1 + F_2 + F_3 + F_4 + F_5}{A}, \quad (4)$$

Where I is the second moment of area with $I = \frac{\pi}{64}(d_o^4 - d_i^4)$, Y is the distance from the neutral axis to the outer surface (0.5 d_o), and A is the cross-section area with $A = \frac{\pi}{4}(d_o^2 - d_i^2)$.

The maximum normal stress criterion and factor of safety (FOS) are expressed as follows:

$$\sigma_{1,2} = \frac{\sigma}{2} \pm \sqrt{\left(\frac{\sigma}{2}\right)^2 + \left(\frac{\tau}{2}\right)^2} \quad (5)$$

Table 1 6 DoF Robot arm parameters.

Parameter	Description	Value	Parameter	Description	Value
d_1	length of the base	45 mm	d_2	offset of joint 2	130 mm
d_3	the offset of joint 3	140 mm	d_4	offset of gripper joint	90 mm
d_5	the offset of gripper joint	115 mm	d_6	offset of gripper joint	82 mm
L_1	length of planar link 1	350 mm	L_2	length of planar link 2	350 mm

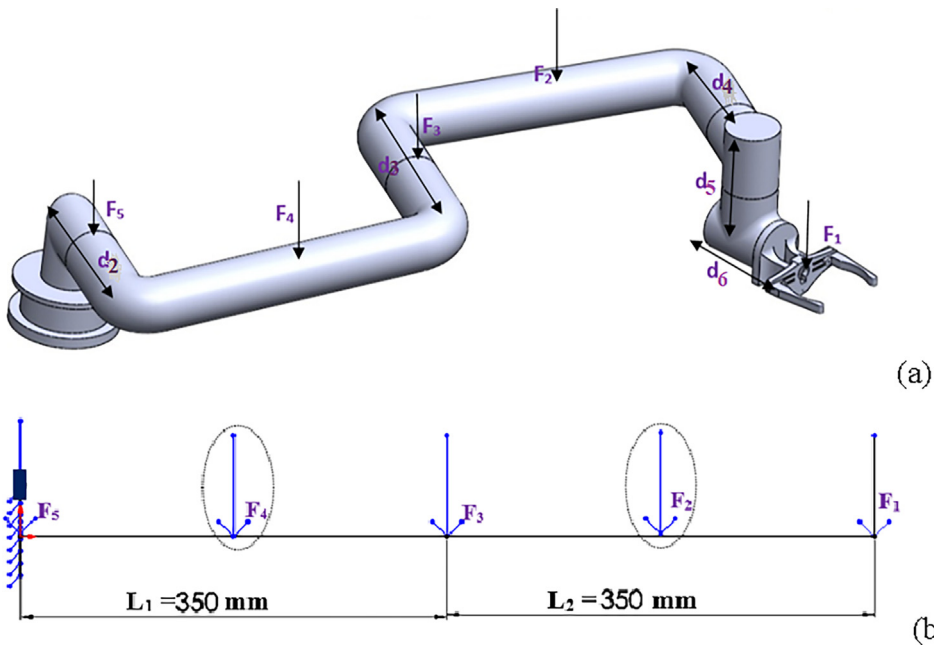


Fig. 3 Static configuration of the robotic arm (a) 3D view, (b) Schematic of the elevation view of applied forces.

Table 2 Materials characteristics of each robot arm design [39,40].

Properties	Structural Steel	Aluminum alloy	Copper	PVC	Magnesium alloy
Density (kg/m ³)	7,800	2,770	8300	1300	1800
Young's Modulus (GPa)	200	69.6	114.6	3.3	45
Yield strength (Mpa)	250	271	280	36	204
Density/strength (kg/m ³ Mpa)	31.2	10.22	29.6	36.1	8.8

$$FOS_{normal} = \frac{S_y}{\sigma_1} \quad (6)$$

Where the shear stress τ , in this case, equals to zero, and S_y is the yield strength.

The maximum stress σ and factor of safety FOS_{Von} based on von Mises theory are given by.

$$\sigma = \sqrt{\frac{(\sigma_1)^2 + (\sigma_2)^2 + (\sigma_1 - \sigma_2)^2}{2}} \quad (7)$$

$$FOS_{Von} = \frac{S_y}{\sigma} \quad (8)$$

The approximate deflections in the x - and y -directions are calculated as follows.

$$y_{maxx} = \frac{(700)^3 F_1 + (525)^3 F_2 + (350)^3 F_3 + (150)^3 F_4}{3EI}, \quad (9)$$

$$y_{maxy} = \frac{(d_2 + d_6)^3 F_1 + d_2^3 F_4 + (d_3 - d_2)^3 \times F_2 + 0.5d_3^3(F_5 + F_3)}{3EI}, \quad (10)$$

where E is the Young's Modulus.

Then, the overall maximum deflection is given so that.

$$y_{max} = \sqrt{y_{maxx}^2 + y_{maxy}^2} \quad (11)$$

The von Mises theory is employed to study the different stresses reflecting the various load capacities acting simultaneously on the links of the robot arm. The FOS estimates the robot's reliability under the applied loads without driving the robot arm to a failure state. The stress analysis is conducted to determine the appropriate type of material for the links of the industrial robotic arm to ensure reliable operation. Fig. 4 reveals the FoSs calculated for a range of outer diameters for different types of materials. Fig. 4 demonstrates that the Copper and Aluminum Alloy withstand stresses for increased diameters, unlike the PVC case, for example. Fig. 5 exhibits the maximum deflections, and it indicates that the PVC displays high deformation when compared with the other types of material. The maximum deflections of the Structural Steel, Aluminum, and Copper types of material are acceptable within an outer diameter range of 40 to 70 mm. These results imply that the Aluminum Alloy could provide a compromise between different features such as high FoS (high reliability), low price, and acceptable total deflection. Additionally, the weight of the Aluminum is 35.5 % less than that of the Structural Steel which decreases the underlying robot weights.

The next step is to determine the outer diameter range that can withstand a range of applied loads with satisfactory FoS for the Aluminum-Alloy. This is because many applications of robots require varying payloads [41].

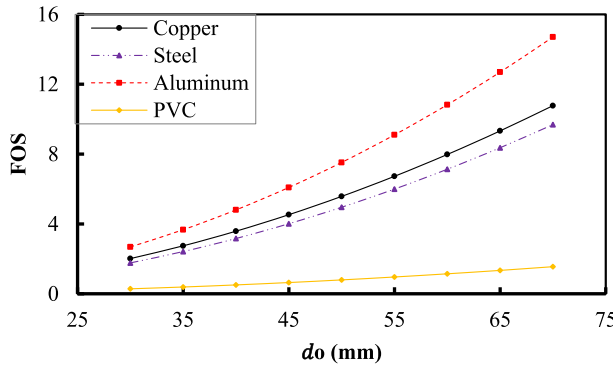


Fig. 4 The von Mises' FOSs for different materials.

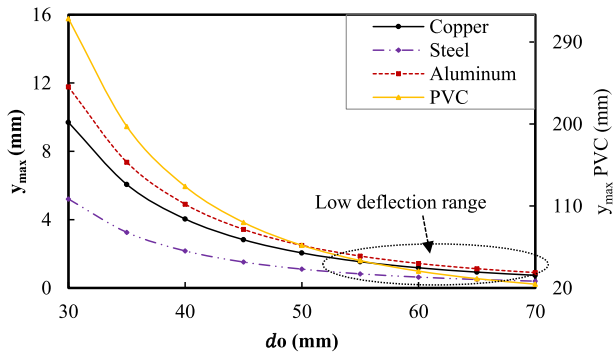


Fig. 5 The maximum deflections of the robotic arm.

This analysis is conducted using a range of mass-loads of 2Kg to 16 Kg. Fig. 6 shows the acceptable range of FoSs corresponding to a range of diameters. The results shown in Fig. 4 to Fig. 7 is multiplied in some coefficients to substitute the absence of the gears and bearings in the analytical analysis and to be more reality. The feasible diameters for different mass-loads are plotted for different FoSs in Fig. 7. These results imply that diameter values selected between 20 mm and 70 mm can withstand mass-loads that range from 2 Kg to 16 Kg with FoSs 2 to 6. For instance, for an outer diameter of 45 mm, if the mass-load varies from 4 Kg to 16 Kg, this would result in FoSs that vary from 6 to 2. High FoS values need to be considered due to the high-reliability requirements of some applications to satisfy the dynamic loads.

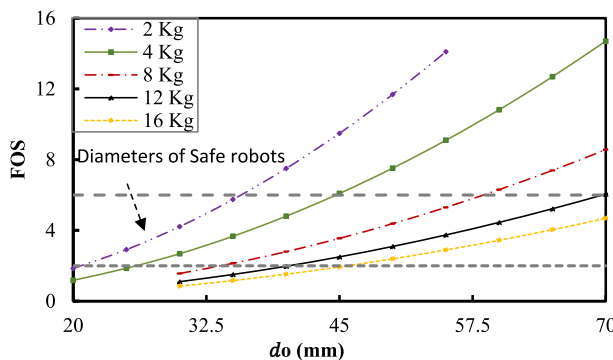


Fig. 6 The FOSs for different mass-loads for Aluminum-Alloy based robot arm.

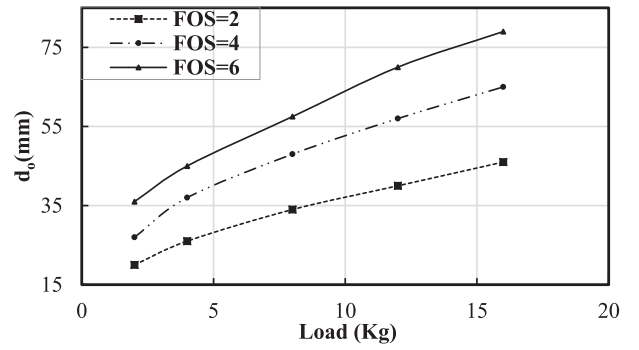


Fig. 7 Load versus outer diameter for Aluminum-Alloy based robot arm.

These results are employed to develop a set of design equations to decide the outer diameter and FoSs required for mass-loads in Kg. Therefore, the data used to generate Figs. 4-7 are used to generate fourth-order polynomials for outer diameter and fifth-order polynomials for the FoS values, and maximum deflection as follows:

$$\begin{aligned} d_o = & -0.002m^4 + 0.0844m^3 - 1.2708m^2 + 10.506m \\ & + 10.429, \end{aligned} \quad (12)$$

$$\begin{aligned} FOS = & -5e^{-13}d_o^5 + 1e^{-9}d_o^4 - 2e^{-6}d_o^3 + 0.0032d_o^2 \\ & - 0.0048d_o + 0.0031 \end{aligned} \quad (13)$$

$$\begin{aligned} y_{max} = & -3e^{-7}d_o^5 + 8e^{-5}d_o^4 - 0.0096d_o^3 + 0.5531d_o^2 \\ & - 16.356d_o + 202.29. \end{aligned} \quad (14)$$

First, the user calculates the outer diameter (mm) in terms of the mass-load m (Kg) and then employs that value to compute the FoS and y_{max} (mm) design parameters.

3.2. Stress analysis using FEM

The industrial robot consists of segments or links that are subject to both rotary and translational motions which imply the existence of simultaneous elastic deformations. In addition to the analytical study of stress analysis, the FE model is constructed, using ANSYS software engine, for the robot to verify the analytical results and to introduce more results of stress analysis. We employed FEM in robot modeling and simulation as stated in previous studies [42].

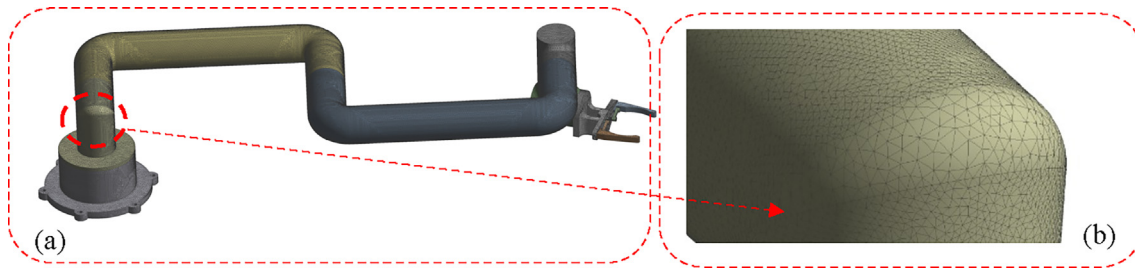
3.2.1. Validation study of FE ANSYS model

To verify the results of our FE ANSYS model we conducted both a mesh convergence study, a comparison with results of a published study, and finally a comparison between FE ANSYS results and analytical results (Table 3).

3.2.1.1. FE model meshing. The preciseness of the FEM results relies on the accuracy of the underlying mesh model. The mesh convergence study requires a high mesh quality and an appropriate element type. The body mesh method is employed to evaluate and measure the mesh accuracy during the mesh analysis. The model meshing is performed using the three nodes triangle element type with 1,116,389 elements and the biggest

Table 3 Comparison between the analytical and FEA approaches.

		Structural Steel	Aluminum Alloy	Copper	PVC
FOS	Analytical	5.9	9	6.72	0.96
	FEA	5.6	8.3	6.17	0.9
y_{max} (mm)		5	7.7	8.1	6.25
	Analytical	0.82	1.86	1.53	50
Error %	FEA	0.87	1.9	1.63	54.25
		5.7	2.1	6.1	7.8

**Fig. 8** Mesh of 3D model of the robot arm (a) robot arm mesh, and (b) mesh details.

element has a size of 1.3 mm to guarantee high mesh accuracy. The total number of nodes is 1,967,221. **Fig. 8(a)** shows the mesh model of the robot arm using ANSYS software. **Fig. 8(b)** shows the type of mesh element (triangle element type) and the mesh density.

3.2.1.2. Comparison of FE ANSYS results with published results. In this section, a comparison was performed between our FEA ANSYS model, and ALTAIR Inspire multibody results of the upper arm of KUKA KR16 [43] to validate our model. The applied force on the upper arm is 832.6 N at the shoulder and 464.2 N at Elbow. **Fig. 9(a)** shows the shoulder and elbow joints of the upper arm link. Also, the shoulder and elbow points are shown in **Fig. 9(b)** and **Fig. 9(c)**. Magnesium alloy is the utilized material for modeling the robot arm. **Fig. 9** demonstrates the maximum stress recorded by Srinivas and Javed [43] was 3.99 MPa and the maximum stress observed by our ANSYS model is 3.96 MPa. **Fig. 9** reveals excellent agreement between the results of our model and the results literature model with an error of 0.75%.

3.2.2. Simulation results

The industrial robot consists of segments or links that are subject to both rotary and translational motions which imply the existence of simultaneous elastic deformations. Herein, the FEM is employed to study the stress analysis of the robot arm where the FEM is deployed in the ANSYS software. The simulations are conducted on a 55 mm diameter robot arm for all the above-mentioned types of material. The simulation accounted for the motors' weights, the gravity of each segment or link, and end-effector loads (same as in the analytical part). Also, the fixed support and free end are specified (see **Fig. 10**). **Fig. 10** reveals the setting in ANSYS of the applied forces, gravity, and fixed support of the robot arm. Where κ refers to the fixed support, G refers to the weight of the robot, F_3 and F_5 refer to the weights of the motors, and F_1 refers to

the payload. **Fig. 11** shows the simulation results of the static analysis for a robot arm that is made of structural steel. **Fig. 11(a)** shows the stress distributions due to the applied static loads using von Mises theory. It is noted that the maximum reported stress is 44.4 MPa at axis 2. While **Fig. 11(b)** reveals that the lowest observed FoS is 5.8. Finally, **Fig. 11(c)** indicates that maximum deformation is 0.87 mm, where it is observed at the gripper. **Table 3** lists the comparison results of the FEM and analytical ones in terms of the maximum deflections (y_{max}) mm and FoSs. These results imply an acceptable match with average errors of 6.7 % and 5.4 %, related to the FoS and maximum deflection results, respectively. This comparison aims to validate the FEM results and to be more convincing. Where FOS is the factor of safety (dimensionless) and y_{max} is the maximum deflection (mm). Error % is the difference between (the FEM results and analytical results *100) relative to analytical results (dimensionless).

4. Vibration analysis

The vibration analysis is concerned with enhancing the dynamic characteristics of the robot arm to avoid working at resonance frequencies. Resonance occurs when the speed(load) frequency of the robotic arm (considering its overall speed combinations) works close to its natural frequencies. At the resonance, the vibration increases and thus might be the cause of the robot failure. This resonance can be avoided either by modifying the excitation frequency due to the robot arm speed or by changing the natural frequency of the robot arm by changing its mass or stiffness parameters.

4.1. Modal decomposition

The excitation frequencies of the industrial robot arm need to be in low values to avoid resonance [32]. In the next section, the speed of the robot will be determined to evaluate the exci-

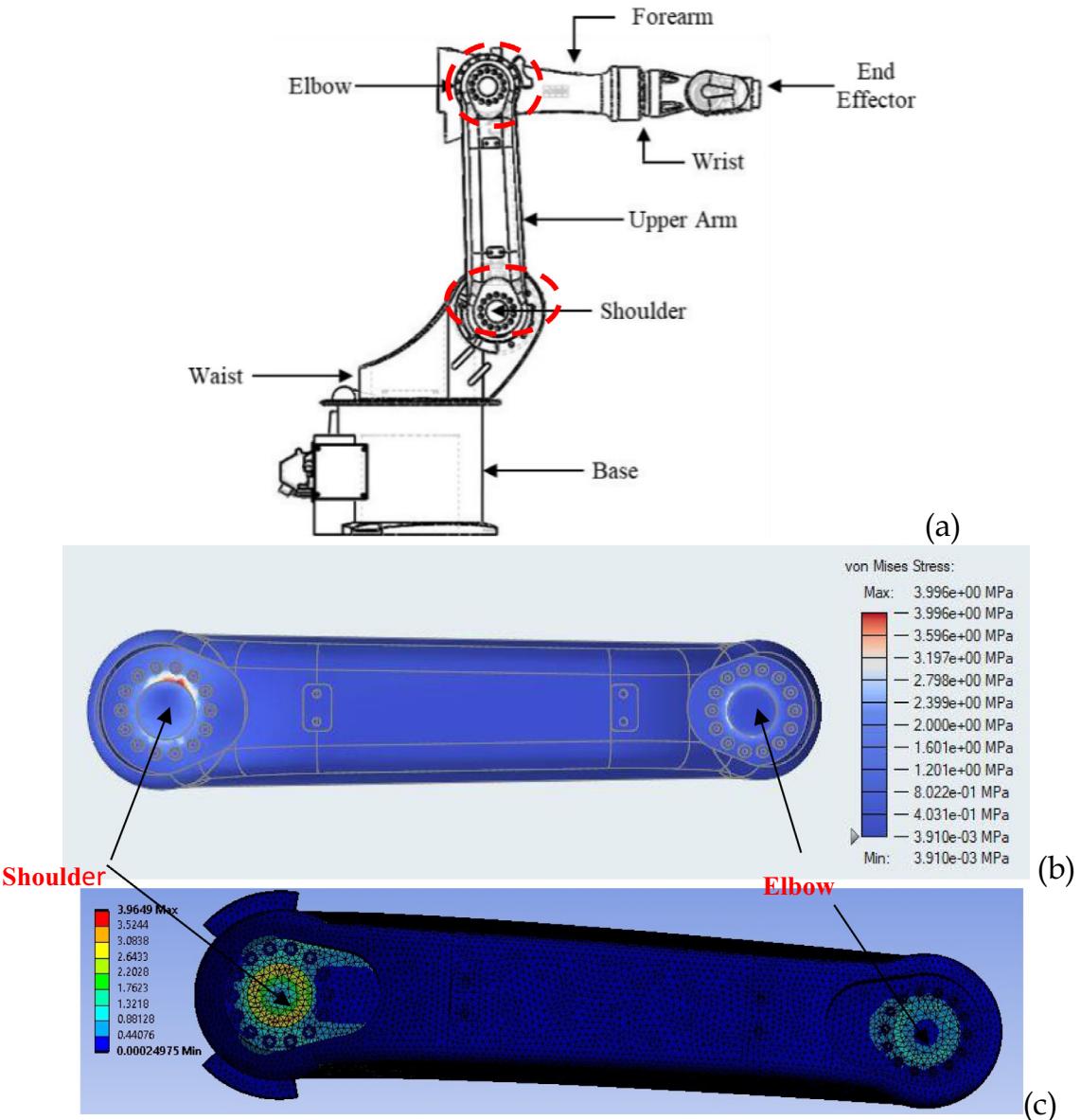


Fig. 9 The stress distribution (a) description of the robot arm (KUKA KR16) (b) Stress distribution of the Upper arm of KUKA KR16 is conducted by [43], and (c) Stress distribution of the Upper arm of KUKA KR16 is conducted by ANSYS in this paper for validation purpose.

tation frequency. The frequencies of excitation are frequencies due to the load (load frequency) or the frequencies resulting from the robot's speed. The resonance occurs when the natural frequency of the robot matches the frequency of speed. At the resonance, the vibration increases, and the probability of failure increases. To escape the same load(speed) frequency as the natural frequency of the system, or nearby frequency doubling occurring, the primary modal design should be conducted to avoid resonance. Also, the natural frequency of the robot arm under small order may be increased by optimizing the mechanical structure, to avoid resonances. Therefore, the goal is to detect the modal parameters, then give references for vibration characteristics analysis, and prediction, and enhance the design of the structural characteristics. The frequencies of excitation must be avoided if their value is near the value of the

natural frequency. During the optimization of the robotic arm, the natural frequencies are increased to stay away from the excitation(speed) frequency. If it is not feasible to change the natural frequencies of the robot arm, the speed (excitation frequency) must be modified to operate far from the natural frequencies.

Modal analysis is conducted using ANSYS software to identify the fundamental natural frequencies and their mode shapes. Fig. 12 presents the natural frequencies for the robot arm made of Aluminum Alloy. Also, the modal analysis reflects the structural dynamic characteristics of the robot arm. Table 4 reveals the values of the first six natural frequencies for the robot arm made of 4 types of material. Kouritem [44] highlighted the importance of investigating the higher modes of vibrations of the piezoelectric energy harvester.

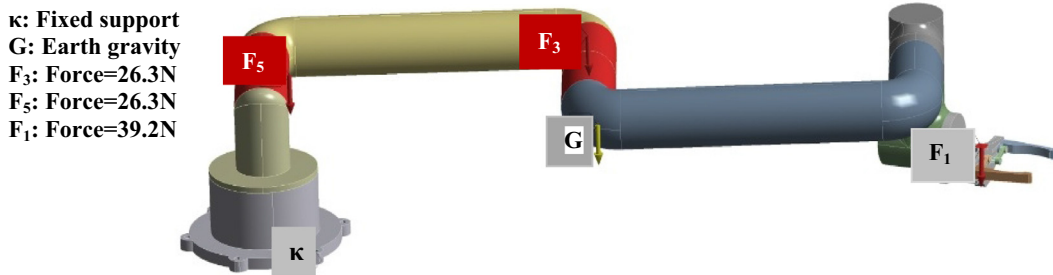


Fig. 10 The setting of the applied forces, gravity and fixed support of the robot arm installed in ANSYS.

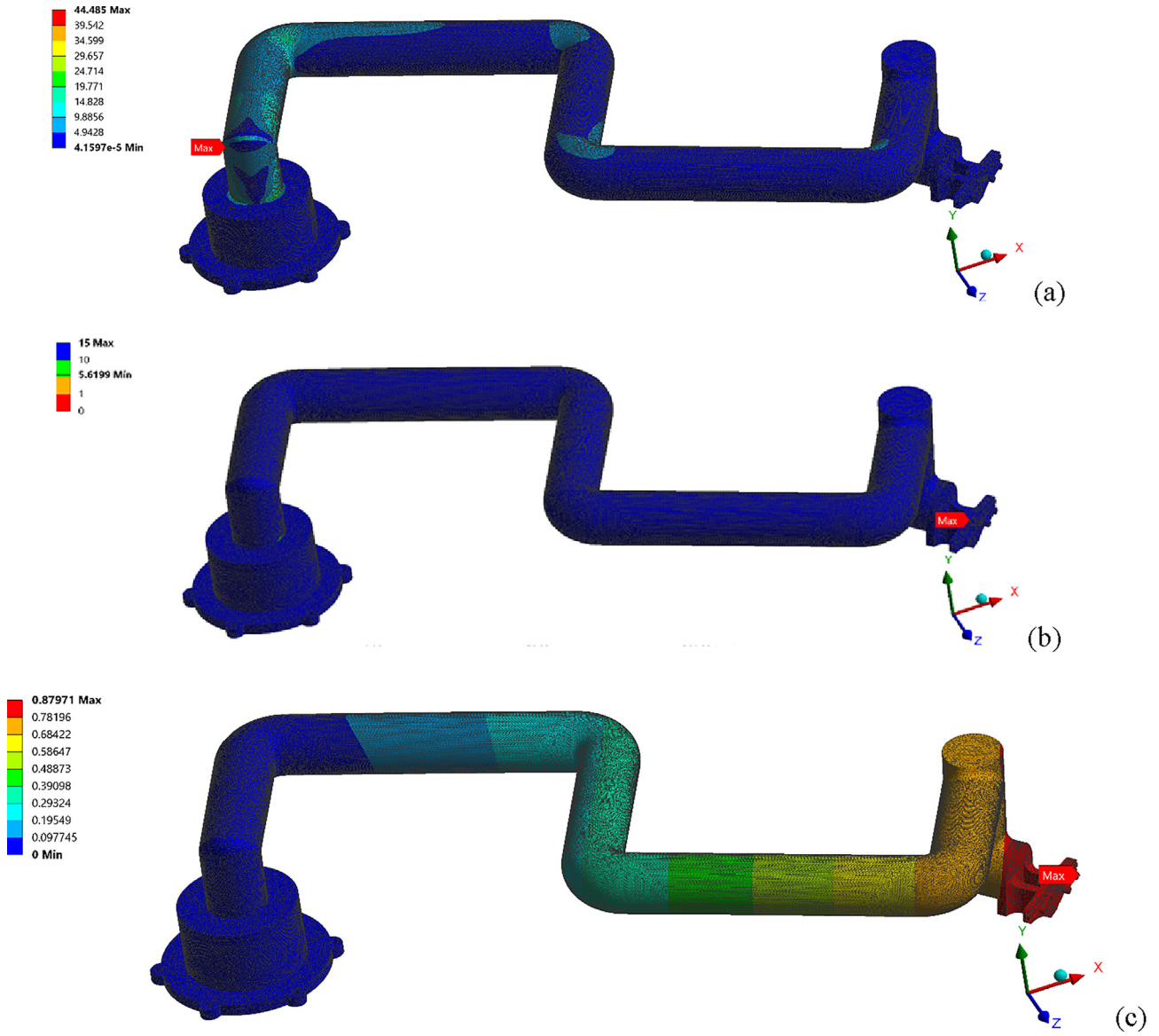


Fig. 11 Stress analysis using FEM for a robot arm made of structural steel (a) stress distribution using von Mises theory (MPa), (b) FoS, and (c) maximum deflection (mm).

The frequencies of the first six modes are recorded as follows 45.9, 49.57, 149.3, 187.7, 214, and 243.7 Hz, respectively. Modes 4 and 5 reflect a twisting behavior while the remaining

modes show bending ones. Based on the speed study, introduced in section 5, the maximum excitation frequency equals 0.795 Hz (5 rad/s). This means that this robot is far away from

its first natural frequency. It can be observed, from the results introduced in [Table 4](#), that the natural frequencies of robot arms made of PVC and Copper are low. So, it is recommended to increase their natural frequencies (i.e., those of the first modes) to avoid working at resonance frequencies. Structural Steel and Aluminum Alloy natural frequencies are higher than the excitation frequency, and their values are very close to each other.

In general, we can increase the natural frequency by increasing the stiffness (k) or decreasing the mass (m) depending on the natural frequency equation $\omega_n = \sqrt{\frac{k}{m}}$ with $k = \frac{3EI}{L^3}$. Considering such relations, the stiffness can be increased by increasing the diameter or decreasing the length. Furthermore,

the length is the most significant parameter for the natural frequency.

4.2. Enhanced design of the robot arm

The maximum stress is evaluated using FEM in the previous section where it is recorded to be 33.46 MPa at the second axis. This section uses the FEM deployed using ANSYS to enhance the design of the robot arm by reducing the weights of selected robot segments following this analysis. Decreasing the overall weight of the robot improves the overall efficiency, as explained earlier. Earlier research ideas suggested decreasing the mass of axis 2 [32], however, this method implies a complicated manufacturing process. The outstanding properties of

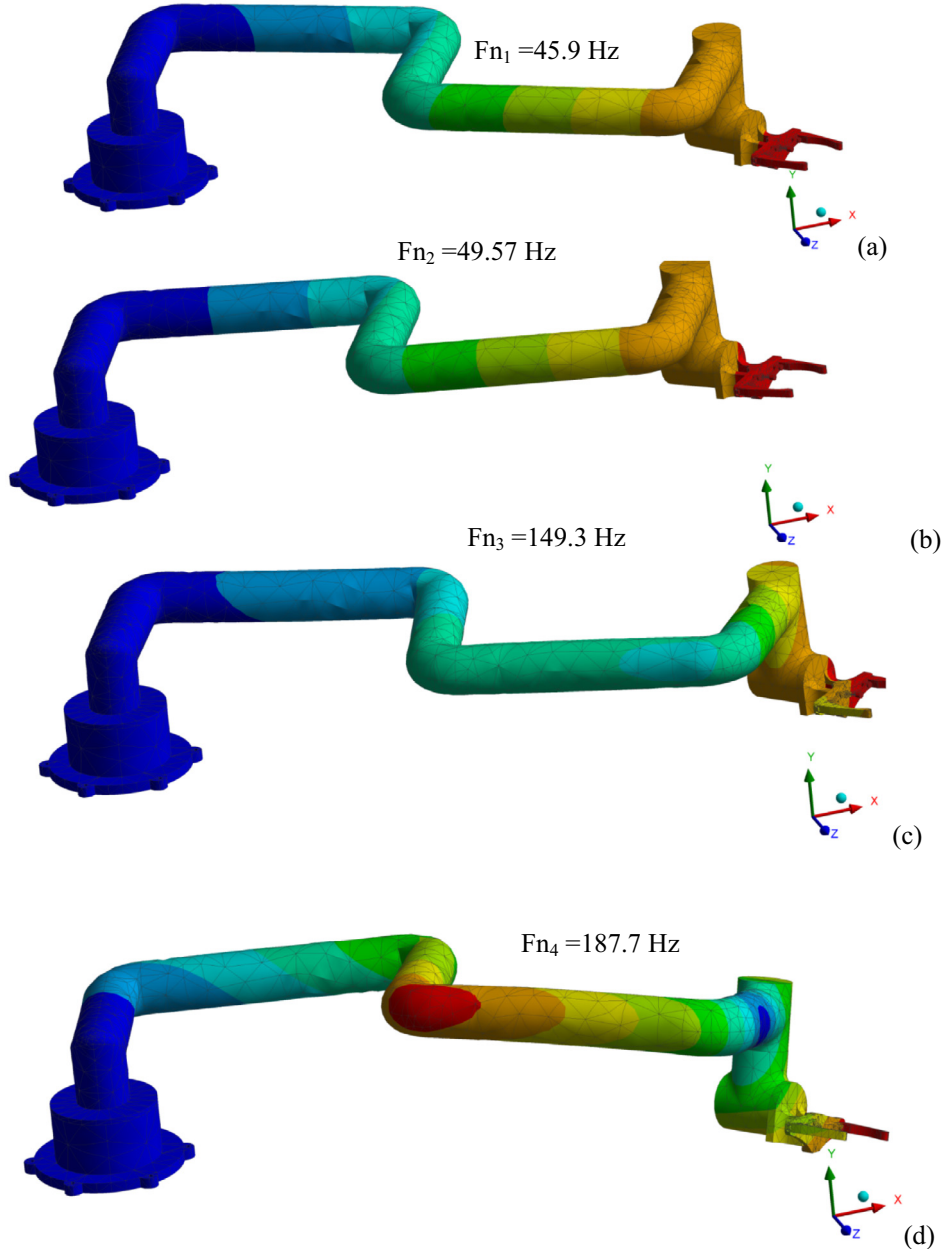


Fig. 12 Mode shapes and natural frequencies of Aluminum-Alloy robot arm, (a) first mode, (b) second mode, (c) third mode, (d) fourth mode, (e) fifth mode, and (f) sixth mode.

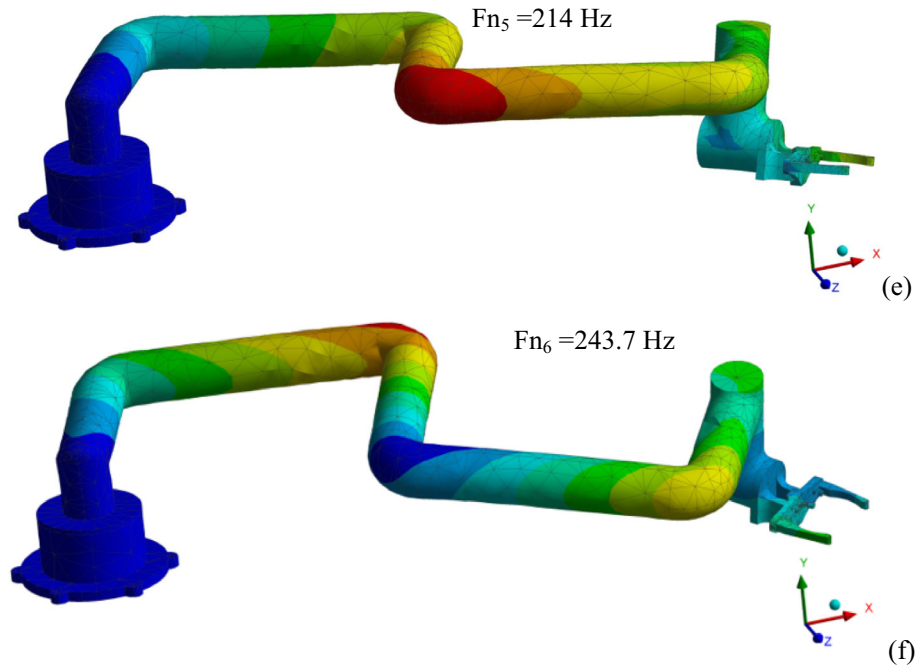


Fig. 12 (continued)

Table 4 First six natural frequencies of the robot arm (Hz) for different materials.

Mode	1st	2nd	3rd	4th	5th	6th
Structural Steel	45.73	49.48	148.5	187.5	213.7	242.8
Aluminum	45.9	49.57	149.3	187.7	214	243.7
Copper	33	35.6	107.4	134.9	153.8	175.3
PVC	9.8	10.5	32.2	39.9	45.5	52.4

Magnesium motivate us to combine it with Aluminum Alloy as a robot material. Although Magnesium is lighter and cheaper than Aluminum alloy, it is weaker in terms of withstanding the stresses [40]. Also, the composite arm can be utilized in the construction of an industrial robot arm and provide an improving fundamental bending frequency [45]. Hence, the segments that experience low stresses are preferred to be structured from Magnesium and those experiencing high stresses use Aluminum Alloy material. In the previous Section, Fig. 11 showed the distribution of the highest and lowest stresses. Thus, the high-stress positions (axis two and base) are constructed of Aluminum Alloy, and the low-stress links (axes 3, 4, 5, and 6) are remade of the low weight Magnesium material. This reduction in mass in the referred segments decreases the weight forces and the associated stresses acting on the robot arm. Consequently, this would increase both the robot arm and motor's life cycles. Fig. 13 highlights the stress distributions for this material combination, where the maximum stress eventually decreases on axis 2 from 33.46 MPa to 31.8 MPa (i.e., by a percentage of 5.21 %). Also, the FOS is increased from 8.3 to 8.79 (i.e., by a percentage of 5.9 %) which implies higher carrying load capacity and lower initial and running costs. It is noted that the FOSs are increased from 8.3 to 8.79 (i.e., by a percentage of 5.9 %) and from 5.6 to 8.79 (i.e., by a percentage of 56.9 %) when the Aluminum Alloy

and Structural Steel material are used, respectively. It is noted that the maximum deflection does not change. Hence, it is possible to decrease the stresses significantly by manufacturing all low-stress segments in the robot arm from Magnesium. Moreover, this Magnesium and Aluminum Alloy combination improve the natural frequencies by increasing the low order modes of natural frequency. It noted that the first six natural frequencies are 51.4, 55.8, 154.5, 192.9, 226.3, and 242 Hz, where the fundamental natural frequency is increased by 12.4 %. This increment in the natural frequencies for the segments of the robot arm drives it away from the resonance undesired performance where it provides a stable robust operation.

5. Realistic analysis of the robot arm

This section aims to highlight the effect of adding reducers and motors to the main body of the robot. The addition aims to make the analysis more realistic. The material of the robot arm utilized in this analysis is Aluminum-Alloy.

5.1. Static stress and vibration analysis

Solidwork is employed to model the robot arm including the drive train (see Fig. 14). Where, the motors, reducers (gear-

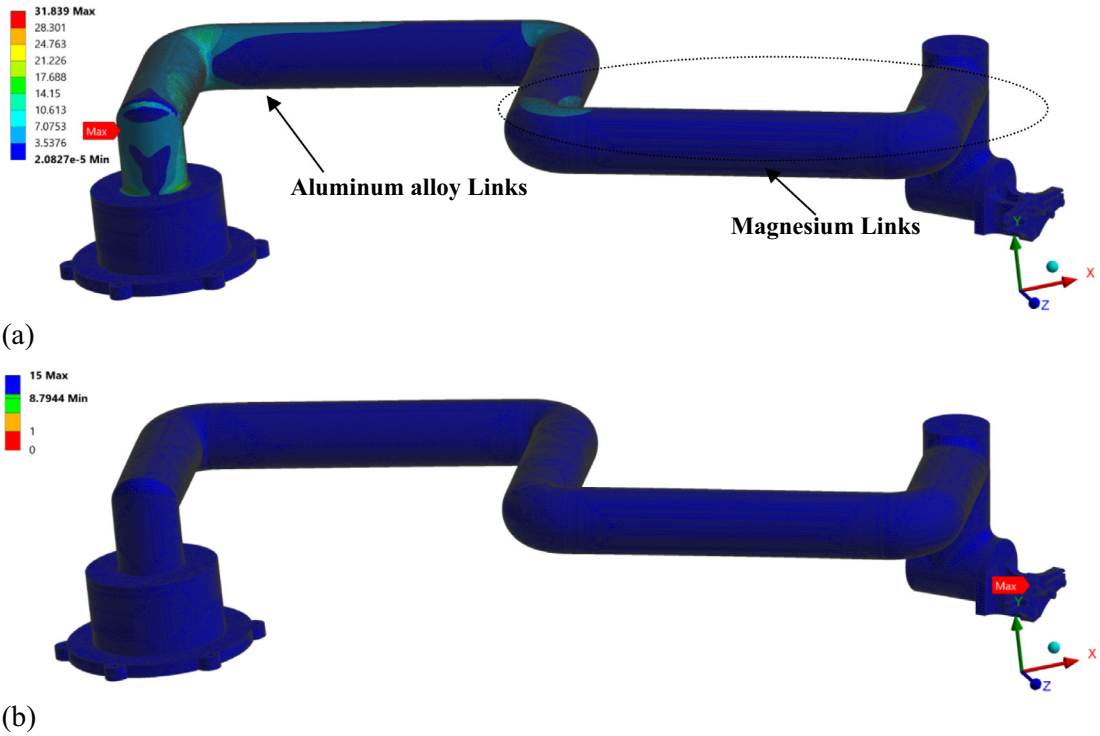


Fig. 13 Stress analysis for the robot of composite material (a) stresses distribution using von Mises (MPa), and (b) FOS.

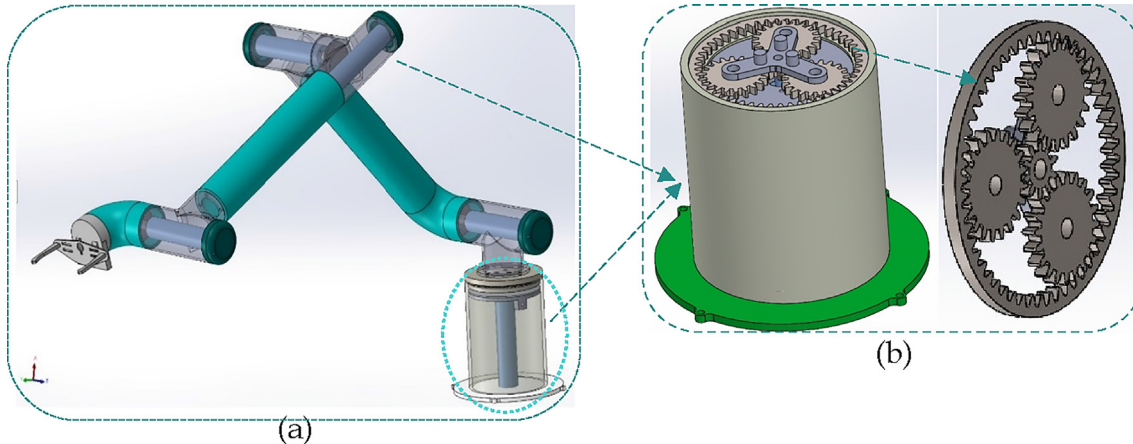


Fig. 14 The modeling of the robotic arm including the drive train by solid works (a) robot arm, and (b) gears and motors.

box), and bearing are added to the robot body. The planetary gear is utilized to provide a high gear ratio in a small space so the weight of the reducer will be lighter than the ordinary reducer for the same reduction ratio. The planetary gear train is suitable for the proposed design (hollow circular cross-section $d = 55$ mm) where the reducer is installed inside the tube as shown in Fig. 14. The ability to transfer high torque capacity is suitable for industrial robot applications. The motors, bearing, and reducers are installed inside the joints. Besides, to maintain the lightweight of the robotic arm, the driving joint is selected to be as close as possible to the mass distribution of each joint. The robotic arm is 6 DOF (6 joints with 6 rotational motions). The axis of rotation of each joint is

specified in ANSYS. Some modifications in the current design related to the joints compared to the previous design have been done to accurately add the gears, and motors to the model. After the modeling and adjusting of the boundary conditions, the static stress analysis of the robot arm including the motors and reducers is conducted. Fig. 15 demonstrates the simulation results of the static analysis for a robot arm at different positions. Fig. 15 shows the stress distributions due to the gear's weights, motors weights, robot weights, and payload. It is observed that the maximum stated stress at 0° of the rotating position (unfavorable position) is 83.6 MPa at axis 2. While Fig. 15 (b) reveals the maximum stated stress at 45° of the rotating position is 83.6 MPa at axis 2. Finally, Fig. 15 (c)

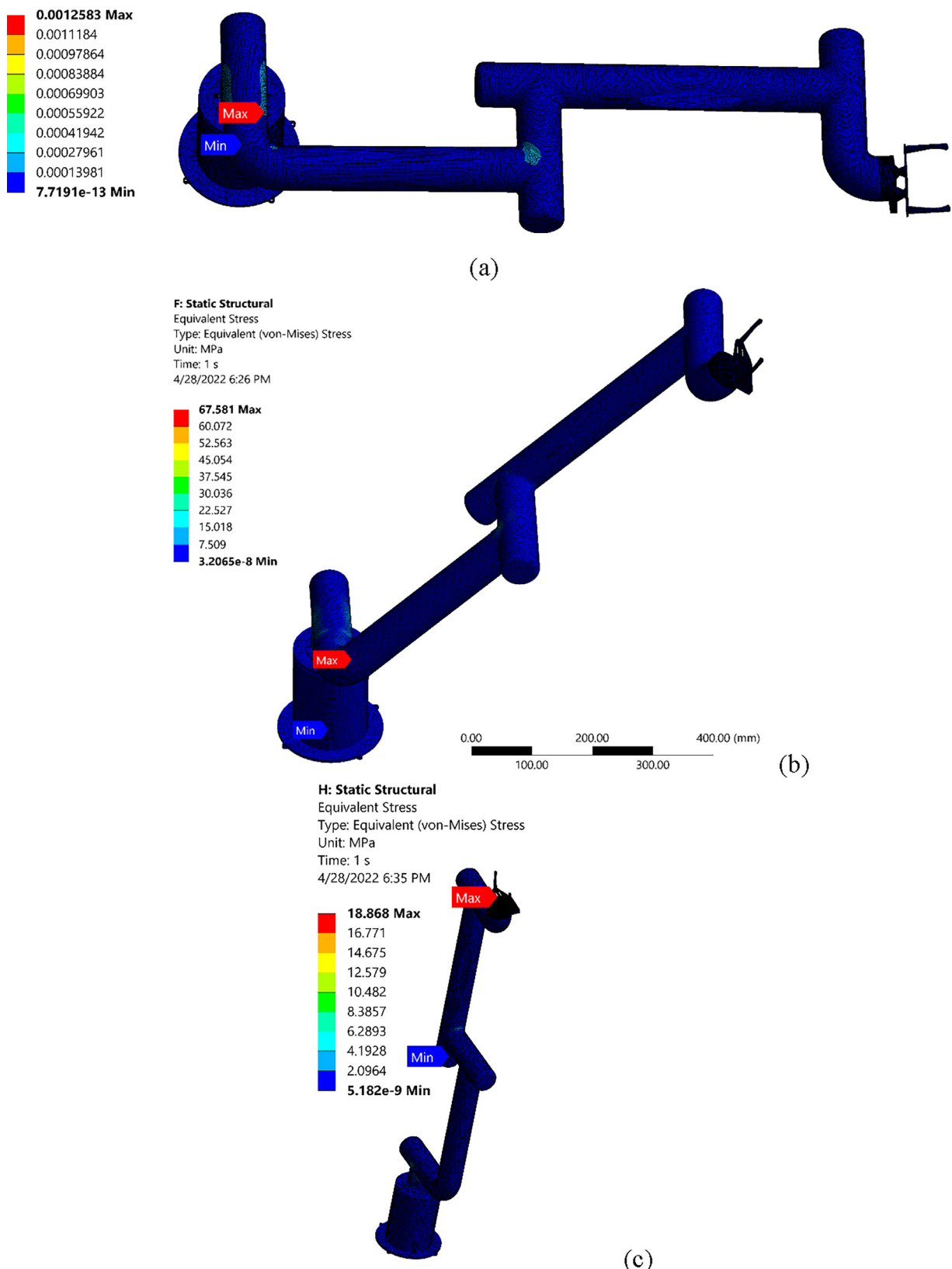


Fig. 15 Simulation of static stress of the robot arm at different positions, (a) at 0° of the rotating position, (b) at 45° of the rotating position, (MPa), and (c) at 90° of the rotating position.

Table 5 The effect of adding the drive system (motors and gears) to the robot body.

	Stress (MPa)	FOS	y_{max} (mm)
Body only	32.5	8.3	1.9
adding drive system	83.6	3.24	3.9

Table 6 The robot arm stresses, FOS, and deflection at different positions.

Angle (position)	Stress (MPa)	FOS(Min)	y_{max} (mm)
0 degrees	83.6	3.24	3.9
45 degrees	67.5	4	2.99
90 degrees	18.8	14.3	0.54

reveals the maximum stated stress at 90° of the rotating position is 83.6 MPa at axis 2. **Table 5** highlights the effect of adding the drive system to the robot body in terms of the maximum stress, maximum deflections mm, and FoSs. The comparison reveals increasing stresses due to the increasing weight of the robot arm and the effect of small connections (stress concentration points). **Table 6** reveals the effect of rotation position(angle) of the robot body in terms of the maximum stress, maximum deflections mm, and FoSs. It is observed that as the rotation angle increases the stress and deflection decrease, while the minimum factor of safety increases. **Fig. 16** shows the natural frequencies for the robot arm including the drive train. **Table 7** reveals the values of the first six natural frequencies for the robot arm including the drive train and the body. The change in the mass and stiffness is the main cause of the natural frequencies. The natural frequencies are increased due to increasing the mass and decreasing the stiffness and thus according to this relation

$\omega_n = \sqrt{\frac{k}{m}}$. Also, the natural frequencies were investigated and evaluated under all rotation positions and found to be constant.

5.2. Dynamic stress and vibration analysis

Dynamic analysis using ANSYS is conducted to make the analysis more realistic. The model is operated in a dynamic environment within the working range and boundary conditions using the transient structural study inside ANSYS. In the first step of the analysis, the boundary conditions of the dynamic analysis are installed in ANSYS. Where, each joint rotates about its axis with speed and inertia moment which depends on the mass and dimensions of the axis. For example, joint 1 rotates from 360 degrees to 270 for 90 degrees in two seconds giving the angular speed of 45 degrees/sec. **Fig. 17** demonstrates the simulation results of the dynamic analysis for a robot arm. **Fig. 17** (a) shows the stress distributions due to the gear's weights, motors weights, robot weights, payload, and inertia force. It is observed that the maximum stated stress is 144.6 MPa. The stresses are evaluated at the worst conditions (maximum inertia and maximum bending). While **Fig. 17** (b) reveals that the lowest observed FoS is 1.55. **Table 8** compares the static and dynamic stresses in terms of the maximum stress Mpa and FoSs. The comparison reveals the increasing stresses (dynamic over the static) due to the inertia force effect. Also, the results highlight the importance of the dynamic investigation of the robot arm, especially if it has a big mass and dimensions. **Table 9** reveals the values of the first six natural frequencies for the robot arm in both free and pre-loaded(payload) force (40 N). It is observed that the frequency decreases in preload case, which confirms earlier studies [46–48]. This result shows the possibility of the varying the robot frequency by varying the preload(payload). The change in the mass and stiffness is the main cause of the natural frequency varying.

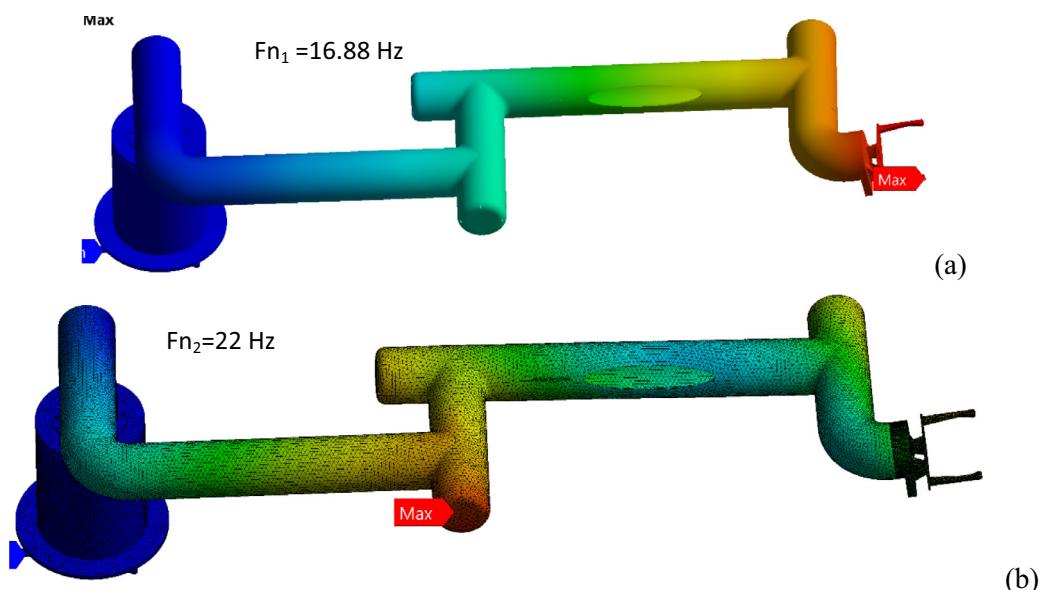
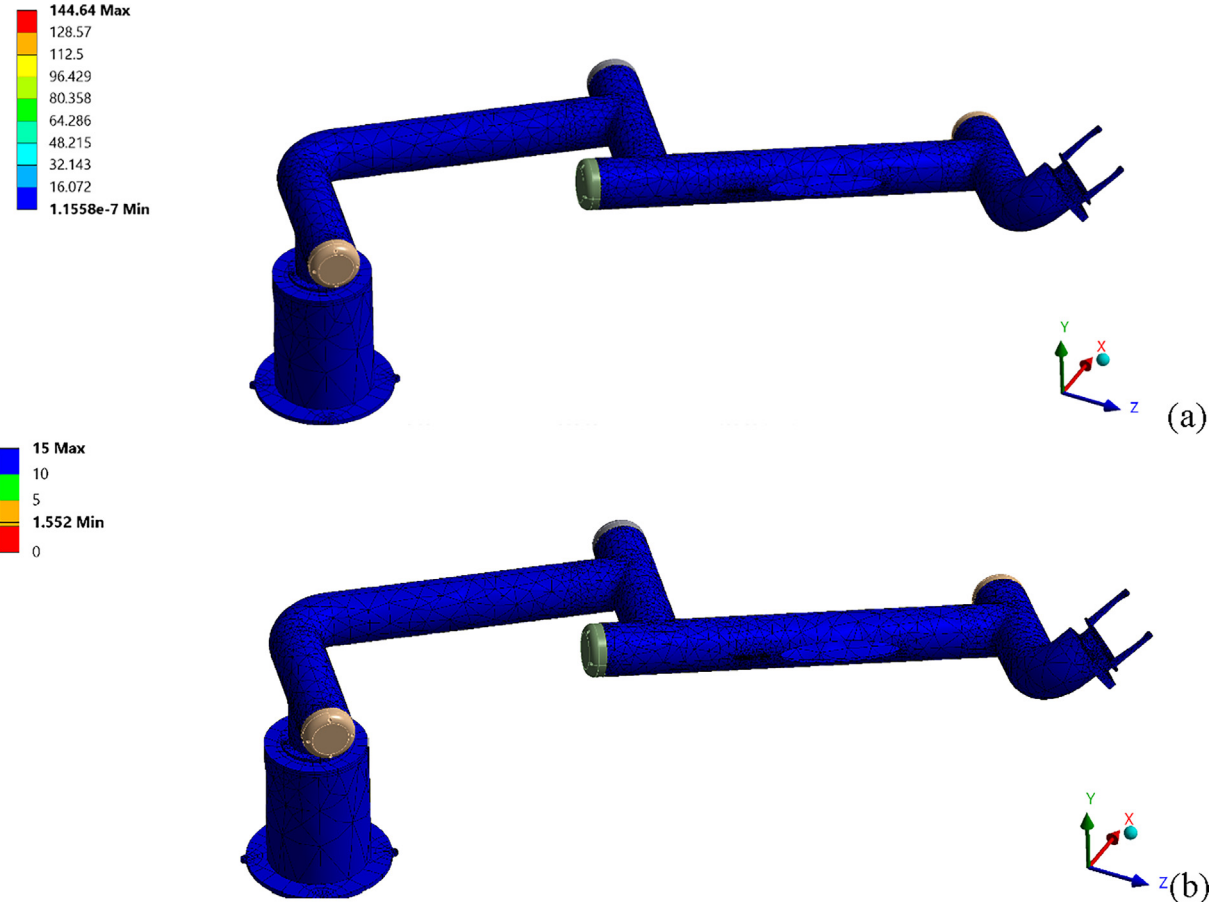
**Fig. 16** Mode shapes and the natural frequencies for the robot arm including the drive train, (a) first mode, and(b) second mode.

Table 7 The effect of adding the drive system on the natural frequencies (Hz).

Mode	1st	2nd	3rd	4th	5th	6th
Body only	45.9	49.57	149.3	187.7	214	243.7
The body including the drive train	16.88	22	92.2	98.9.7	144	155.1

**Fig. 17** Dynamic stress analysis of a robot arm including the drive train (a) stress distribution using von Mises theory (MPa), (b) FoS.**Table 8** The comparison of static and dynamic stresses.

	Stress (MPa)	FOS
Static	83.6	3.24
Dynamic	144.6	1.55

Table 9 The natural frequencies free and preloaded (dynamic case) (Hz).

Mode	1st	2nd	3rd	4th	5th	6th
Free	16.88	22	92.2	98.9.7	144	155.1
Preloaded	8.58	9.88	65.38	71.33	84.9	93.3

6. Motion optimization

6.1. Equations of motion

In the sequel, the motion optimization of the planner links (axes 2 and 3) using the Genetic Algorithm (GA) is considered. The motion optimization of the other links is negligible due to their low contributions to the overall improvement. Hence, the more influential links (i.e., axes 2 and 3) are considered to relax

the number of computations needed by the GA. The maximum stresses and torques are observed on axis 2, so Axis 1 and the gripper motions axes (4, 5, and 6) will not be considered. Furthermore, the lengths of axes 1, 4, 5, and 6 are negligible when compared with the lengths of axes 2 and 3. The end effector is assumed to move along a specified trajectory and the goal is to minimize the consumed power during that motion. This is done by optimizing a cost or utility function that is dependent on the angular velocities of the links. This would minimize the

kinetic energy, and thus reduce the torque applied to the robot arm. Each link i has a mass m_i , length L_i , motor hub inertia I_{hi} , and moment of inertia I_i . The equation of motion for each link i using Lagrange dynamics can be expressed as follows.

$$Q_i = \frac{d}{dt} \left(\frac{\partial L}{\partial \dot{\theta}_i} \right) - \frac{\partial L}{\partial \theta_i}, \quad (15)$$

where L refers to a Lagrange function and it is equal to the difference between the total Potential Energy (P.E.) and Kinetic Energy (K.E.). Q_i is a generalized force that is associated with the applied torques at each joint i . In this development, subscript 1 refers to axis 2, and 1 indicates the first planner link, and subscript 2 refers to axis 3. The potential and kinetic energy of the robot arm can be expressed as [49]:

$$P.E = \frac{m_1 g L_1}{2} S_1 + m_2 g \left(L_1 S_1 + \frac{L_2}{2} S_{12} \right) \quad (16)$$

$$\begin{aligned} K.E = & \dot{\theta}_1^2 \left(\frac{1}{6} m_1 L_1^2 + \frac{1}{6} m_2 L_2^2 + \frac{1}{2} m_2 L_1^2 + \frac{1}{2} m_2 L_1 L_2 C_2 \right) \\ & + \dot{\theta}_2^2 \left(\frac{1}{6} m_2 L_2^2 \right) + \dot{\theta}_1 \dot{\theta}_2 \left(\frac{1}{3} m_2 L_2^2 + \frac{1}{2} m_3 L_1 L_2 C_2 \right) \end{aligned} \quad (17)$$

Substituting Eqs. (16) and (17) into Eq. (15) and after simplifications, the equations of motion can be expressed as:

$$\begin{bmatrix} T_1 \\ T_2 \end{bmatrix} = \begin{bmatrix} M_{11} & M_{12} \\ M_{21} & M_{22} \end{bmatrix} \begin{bmatrix} \ddot{\theta}_1 \\ \ddot{\theta}_2 \end{bmatrix} + \begin{bmatrix} C_{11} & C_{12} \\ C_{21} & C_{22} \end{bmatrix} \begin{bmatrix} \dot{\theta}_1^2 \\ \dot{\theta}_2^2 \end{bmatrix} \\ + \begin{bmatrix} R_{11} R_{12} \\ R_{21} R_{22} \end{bmatrix} \begin{bmatrix} \dot{\theta}_1 \dot{\theta}_2 \\ \dot{\theta}_1 \dot{\theta}_2 \end{bmatrix} + \begin{bmatrix} G_{11} \\ G_{22} \end{bmatrix}. \quad (18)$$

where $T = \begin{bmatrix} T_1 \\ T_2 \end{bmatrix}$, $M = \begin{bmatrix} M_{11} & M_{12} \\ M_{21} & M_{22} \end{bmatrix}$, $C = \begin{bmatrix} C_{11} & C_{12} \\ C_{21} & C_{22} \end{bmatrix}$, $R = \begin{bmatrix} R_{11} R_{12} \\ R_{21} R_{22} \end{bmatrix}$, and $G = \begin{bmatrix} G_{11} \\ G_{22} \end{bmatrix}$ are the torque, mass inertia matrix, Centrifugal matrix, Coriolis matrix, and gravity matrix, respectively [50]. The coefficient values of these matrices are listed in Appendix.

6.2. Optimization using GA

A Genetic Algorithm is a search technique that relies on natural selection and the mechanics of natural genetics. It reflects an artificial endurance of the healthiest genetic operators detracted from nature to form a remarkably robust search mechanism. The GA provides a feasible solution, where it is not needed to evaluate the Jacobian matrix and it can use only the forward kinematic equations. Further, the joint rotation constraints are treated in a direct manner [51]. The angular displacements (trajectory) of each joint i of the two planar links can be expressed as a 4th order polynomial equation [52]:

$$\theta_i = a_{4i} t^4 + a_{3i} t^3 + a_{2i} t^2 + a_{1i} t + a_{0i}, \quad (19)$$

Where a_{4i} , a_{3i} , a_{2i} , a_{1i} , and a_{0i} are coefficients selected to satisfy the boundary conditions of the specified mission and optimize an objective function, a_{1i} depends on the initial angular velocity, while a_{0i} depends on the initial angular displacement. Thus, a_{1i} and a_{0i} are equal to zero for most industrial robots. The other boundary conditions are listed as follows:

$$\theta_1(T_f) = 1 \text{ rad}, \theta_2(T_f) = (1.5 \text{ or } 1) \text{ rad}, \text{ and } \theta_i(0) = 0 \quad (20)$$

Table 10 The angular displacements coefficients using GA optimization techniques.

Coefficient	Value	Coefficient	Value
a_{41}	-8.18E-10	a_{42}	5.37E-10
a_{31}	-2.50E-4	a_{32}	-3.75E-4
a_{21}	0.0075	a_{22}	0.0113

$$\dot{\theta}_1(T_f) = 0, \dot{\theta}_2(T_f) = 0, \text{ and } \dot{\theta}_i(0) = 0 \quad (21)$$

Where T_f refers to the specified (final) time of the mission.

The objective is to optimize the motion of the robot arm following a specified trajectory under the constraints to minimize the overall consumed power. The objective function used herein is inspired by [53] and formed such that.

$$\min Power = \sum |T_i \dot{\theta}_i|. \quad (22)$$

It penalizes the product of the torques applied at the planner joints and the angular velocities of the joints during the execution of the mission to guarantee optimized mission fulfillment. The torque depends on the angular displacements and velocities as mentioned in Eq. (18). The GA optimizes six coefficients of the angular polynomial mentioned in Eq. (19). The constraints are the boundary conditions of the angular displacements and velocities listed by Eqs. (20) and (21).

6.3. Simulation results

The analysis is conducted for the robot arm made of Aluminum Alloy. The optimization and simulations were performed using the parameters of the analytical section as follows: $m_1 = m_2 = 2.6$ Kg (weight of the link, motor, and reducers) and $L_1 = L_2 = 0.35$ m. Since the consumed power is reluctant to the mission time, a time of 20 sec is considered. The trajectory starts with $(0, 0)$ joint angles and ends with $(1, 1.5)$ angles in case 1 and $(1, 1)$ in case 2. The coefficients of the angular displacements that meet the optimized objective function are listed in Table 10. As stated earlier, the values of a_{1i} and a_{0i} are zeros following the initial conditions of the displacements and the velocities. The simulations were performed at two trajectory times (0.5 and 20 s) to display the effect of the trajectory time on the torque and power. Fig. 18 displays the time response of displacements, velocities, torques, and power against the total mission time of 0.5 s. Fig. 19 reveals the time response of displacements, velocities, torques, and power against the total mission time of 20 s. It is observed that velocity, acceleration, inertia torque, total torque, and power are very high for the mission time of 0.5 s. The velocity reaches 5 rad/s so the resonance frequencies must be checked in this case as mentioned in the previous section. While the power highly decreases for the mission time of 20 s due to decreasing in velocity, acceleration, and inertia torque. Fig. 20 highlights the optimized consumed energy versus the trajectory time. The applied torque and consumed power have shown an overall reduction in the period between 0.5 Sec and 5 Sec while the greatest drop happens during the first two seconds and the slighter drop occurs during the following 3 Secs. The consumed power is negligible later towards the end of the mission time. The power is observed to be 79 Watts after 0.5 Sec and 4

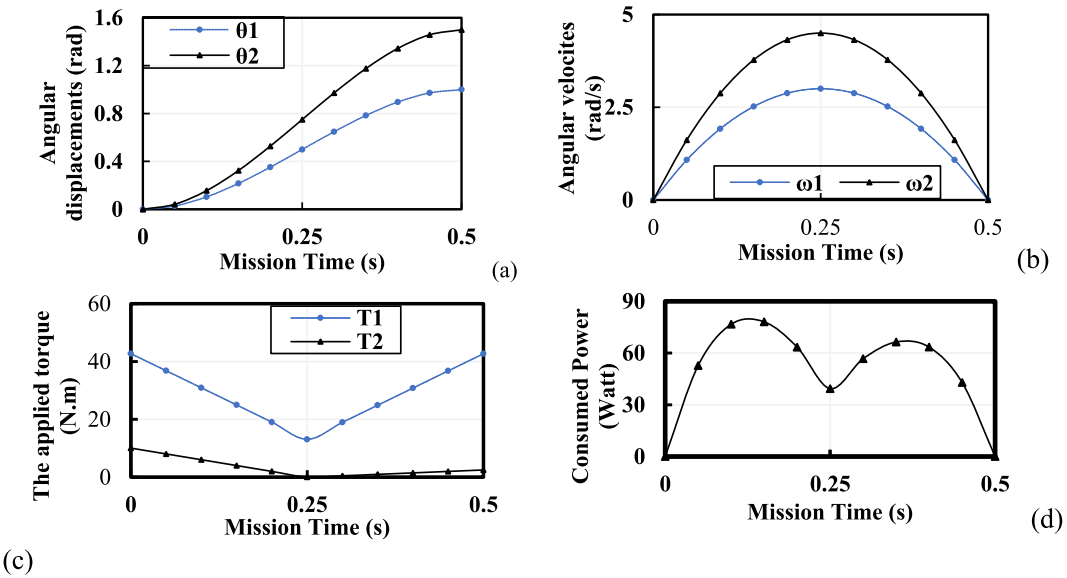


Fig. 18 The simulation results at mission time equal 0.5(s) (a) Angular displacements, (b) Angular velocities, (c) The applied torque, (d) Consumed Power.

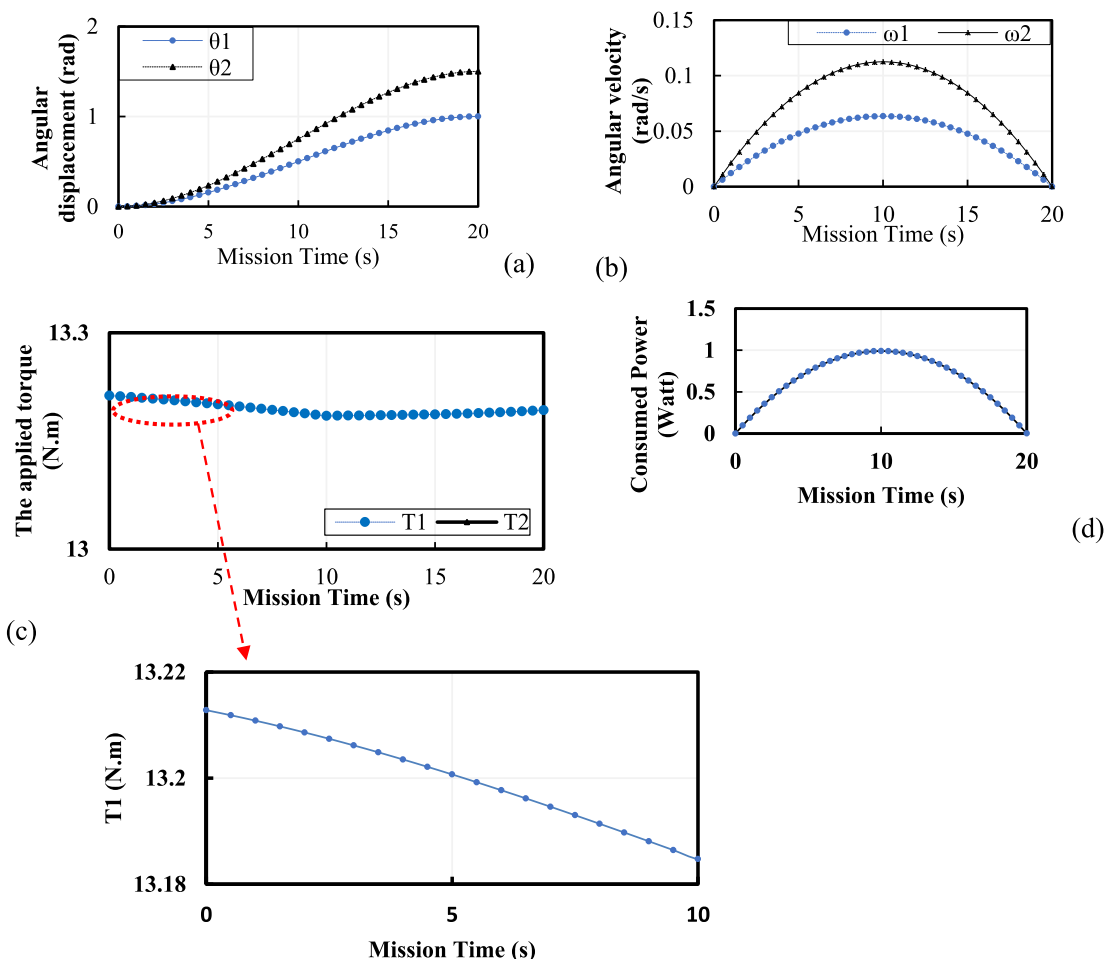


Fig. 19 The simulation results at mission time equal to 20 (s) (a) Angular displacements, (b) Angular velocities, (c) The applied torque, (d) Consumed Power.

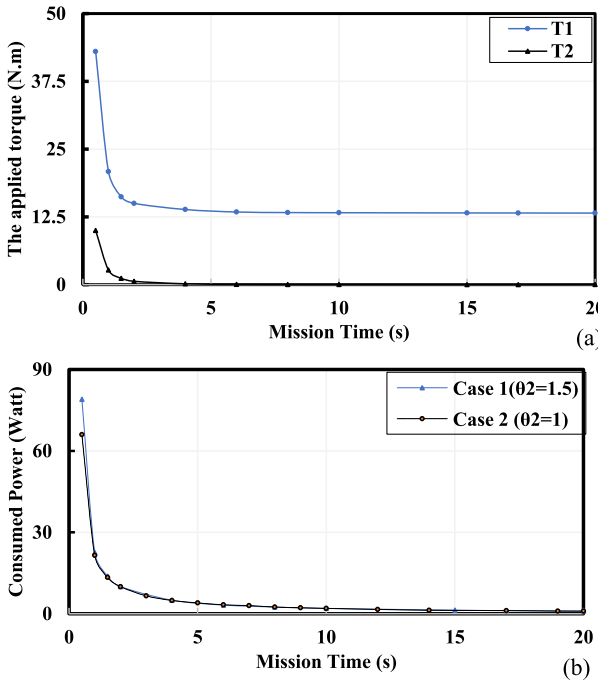


Fig. 20 The applied torques and consumed power during the optimized mission using GA (a) applied torque, (b) Consumed power at different end conditions.

Watts after 5 Secs with a 94.9 % reduction in power consumption at ($\theta_2(T_f) = 1.5$). Therefore, it is recommended to let the mission period 5 Secs. For case (2) as $\theta_2(T_f) = 1$, the power decreases slightly to be 66 Watt after 0.5 Sec while is the same as case 1 at the remaining times. This means that increasing the rotation angle increases the power only for the very small mission time. Fig. 20(a) shows the torques of two joints (for 20 Sec). The results exhibit a decrease in the torque of the first joint (i.e., at axis 2) and show that higher-torque values are needed initially to overcome the friction and the high inertia of the small mission time. The torque of the first joint is high compared with that of joint 2 where joint 1 (axis 2) is located away from the end effector which makes the required torque and associated stress very high at joint 1 (axis 2).

6.4. Kinematic analysis

This section incorporates the Denavit–Hartenberg (D-H) and Robo-Analyzer tools to find the forward and inverse kinematics of the robot arm. The kinematic equations of the robot arm describe the relations between the position, velocity, and acceleration without considering the applied forces or torques. The Denavit–Hartenberg (D-H) describes the kinematic equations of the robot arm using four parameters to assign the reference frame for the links and the associated joints. Each joint i is characterized by two parameters, the length a_i and the twist angle α_i . The twist angle α_i refers to the axis-twist angle of two adjoining joints. Furthermore, the joints can be represented by two parameters: the link offset d_i , which refers to the distance from one link to the next link along the axis of

Table 11 The D-H dynamic parameters of the robot-arm coordinate frame.

Variable	α (Twist angle)	a (Link length) (m)	d (Link offset) (m)	T_n
θ_1	90	0	0.045	0T_1
θ_2	0	0.35	0.13	1T_2
θ_3	0	0.35	0.14	2T_3
θ_4	90	0	0.09	3T_4
θ_5	90	0	0.115	4T_5
θ_6	0	0	0.082	5T_6

the joint, and joint angle θ_i , which is the rotation of one link relative to the next link about the joint axis [54].

The forward kinematics determines the orientation and position of the end-effector using a set of joint angles. Hence, it is important to determine the end effector positions in terms of the joint's angles. In contrast, the inverse kinematics equations find the angles of the joints to reach a specific end-effector position. The robotics users may use the alternative solutions introduced by the inverse kinematics. Also, the forward kinematics introduce many end-effector positions for high flexibility.

The Robo-Analyzer has been used to show the kinematic analysis of robots where Table 11 lists the D-H parameters of the robot arm such as twist angle, link length, and link offset [55]. Fig. 21 reveals the original robot coordinate system and the robot-arm trajectory at angles ($\pi/2, \pi/2, -\pi/2, 0, 0, 0$) using Robo Analyzer software. The trajectory signifies the desired position evolutions of the end effector.

The following matrices are employed to obtain the forward and inverse kinematics and describe the expected rotation and translation of each joint. These calculated for any two neighbor joints at angles ($\pi/2, \pi/2, -\pi/2, 0, 0, 0$) as follows:

$$\begin{aligned} {}^0T_1 &= \begin{bmatrix} 0 & 0 & 1 & 0 \\ 1 & 0 & 0 & 0 \\ 0 & 1 & 0 & 0.045 \\ 0 & 0 & 0 & 1 \end{bmatrix}, {}^1T_2 = \begin{bmatrix} 0 & -1 & 0 & 0 \\ 1 & 0 & 0 & 0.35 \\ 0 & 0 & 1 & 0.13 \\ 0 & 0 & 0 & 1 \end{bmatrix}, \\ {}^2T_3 &= \begin{bmatrix} 0 & 1 & 0 & 0 \\ -1 & 0 & 0 & -0.35 \\ 0 & 0 & 1 & 0.14 \\ 0 & 0 & 0 & 1 \end{bmatrix}, \\ {}^3T_4 &= \begin{bmatrix} 1 & 0 & 0 & 0 \\ 0 & 0 & -1 & 0 \\ 0 & 1 & 0 & 0.09 \\ 0 & 0 & 0 & 1 \end{bmatrix}, {}^4T_5 = \begin{bmatrix} 1 & 0 & 0 & 0 \\ 0 & 0 & -1 & 0 \\ 0 & 1 & 0 & 0.115 \\ 0 & 0 & 0 & 1 \end{bmatrix}, \\ \text{and} {}^5T_6 &= \begin{bmatrix} 1 & 0 & 1 & 0 \\ 0 & 1 & 0 & 0 \\ 0 & 0 & 1 & 0.082 \\ 0 & 0 & 0 & 1 \end{bmatrix} \end{aligned}$$

The product of these matrices provides the total transformation matrix of the end effector relative to the base (EE configuration) such that:

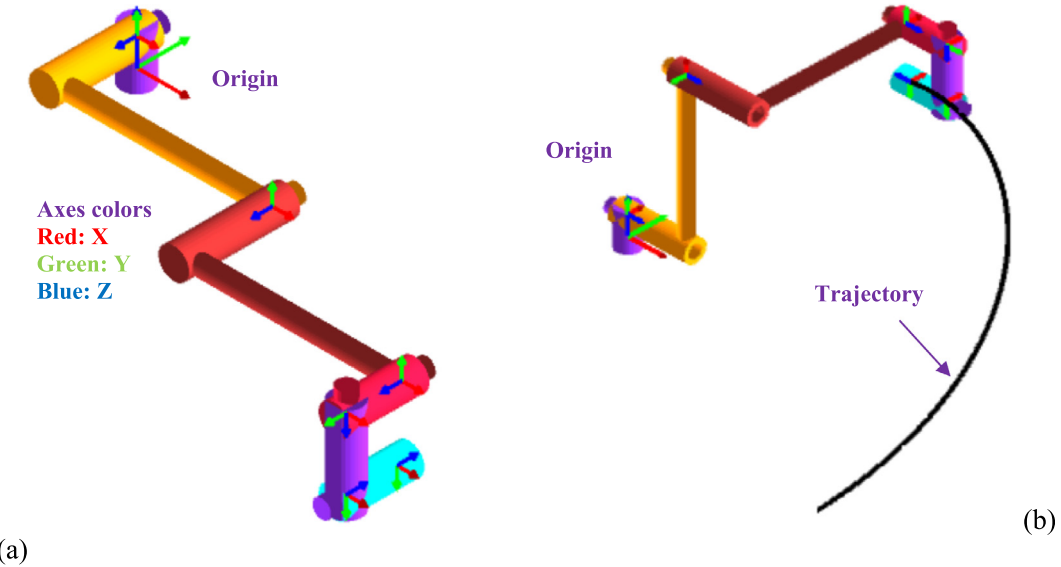


Fig. 21 (a) Robot coordinate system using Robo-Analyzer, (b) robot trajectory at angles ($\pi/2, \pi/2, -\pi/2, 0, 0, 0$).

Table 12 The end effector positions (m) correspond to different values of six joints (rad).

Case	θ_1	θ_2	θ_3	θ_4	θ_5	θ_6	X	Y	Z
1	$\pi/3$	$\pi/3$	$\pi/3$	$\pi/3$	$\pi/3$	$\pi/3$	0.24	-0.221	0.766
2	$\pi/3$	$\pi/3$	$\pi/3$	0	0	0	0.29	-0.052	0.7
3	$\pi/3$	$\pi/3$	$\pi/3$	$\pi/6$	$\pi/6$	$\pi/6$	0.261	-0.125	0.77
4	$\pi/2$	$\pi/2$	$\pi/2$	$\pi/6$	$\pi/6$	$\pi/6$	0.288	-0.44	0.47
5	$\pi/2$	$\pi/2$	$-\pi/2$	$\pi/6$	$\pi/6$	$\pi/6$	0.288	0.44	0.315
6	π	$\pi/2$	$-\pi/2$	$\pi/6$	$\pi/6$	$\pi/6$	-0.443	0.288	0.315
7	$\pi/2$	$\pi/2$	$-\pi/2$	$\pi/3$	$\pi/3$	$\pi/3$	0.319	0.485	0.399
8	$\pi/2$	$\pi/2$	$-\pi/2$	0	0	0	0.278	0.35	0.28
9	$\pi/2$	$\pi/2$	$\pi/2$	$\pi/2$	$\pi/2$	$\pi/2$	0.36	-0.465	0.313

$$OT6 = OT11T22T33T44T55T6 = \begin{bmatrix} 0 & 0 & -1 & 0.278 \\ 1 & 0 & 0 & 0.35 \\ 0 & -1 & 0 & 0.28 \\ 0 & 0 & 0 & 1 \end{bmatrix} \quad (25)$$

Table 12 shows the end effector positions corresponding to different joint angles using the forward kinematic analysis by Robo-Analyzer. The reprogrammable robot arm allows the

users to select the proper angles to reach the desired positions. It is necessary to determine all alternative solutions to reach the desired positions of the end effector using inverse kinematics. Figs. 22-24 reveal the change in the angular displacements, velocities, and accelerations. The simulations are conducted using Robo-Analyzer based on the quintic function (fifth-order polynomial function). The results demonstrate the smooth performance of the robot-arm as can be seen from the displacements behavior of the six joints. It is noted that

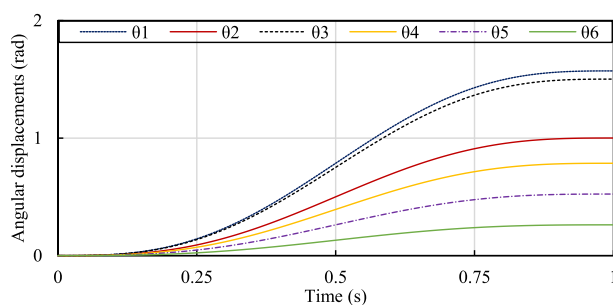


Fig. 22 The angular displacements of the joints using forward kinematics at angles ($\pi/2, 1, 1.5, \pi/4, \pi/6, \pi/12$).

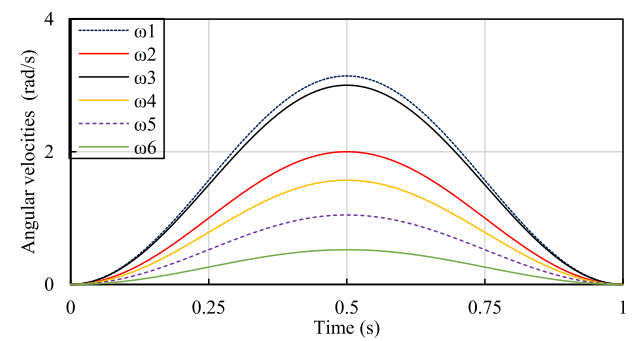


Fig. 23 The angular velocities displacements of the joints using forward kinematics at angles ($\pi/2, 1, 1.5, \pi/4, \pi/6, \pi/12$).

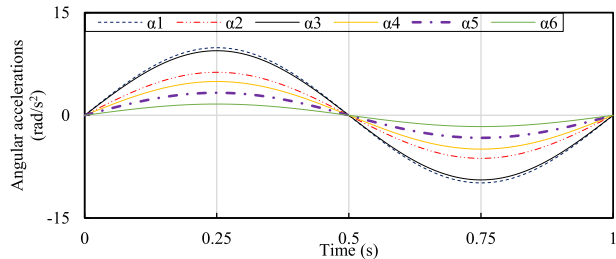


Fig. 24 The angular accelerations of the joints using forward kinematics at angles ($\pi/2$, 1, 1.5, $\pi/4$, $\pi/6$, $\pi/12$).

some of the joint displacements increase up to the maximum values while some other decrease towards their minimum limits at the end of the mission. On another side, the angular velocities take sinusoidal forms where the maximum velocities of the joints occur at the mid of the planned mission. **Tables 13 and 14** demonstrate the inverse kinematics analysis of two positions of the robot arm. **Table 13** presents eight possible alternatives to reach end-effector position (0.378, 0.35, 0.28). **Table 14** provides ten alternatives to reach end-effector position (-0.443, 0.288, 0.315). It is preferable to select the most efficient-wise solution (i.e., among the alternatives) in terms of the required power to reach the desired end-effector position.

7. Conclusions

This work introduced a set of design mechanisms to optimize the performance of industrial robot arms subject to different

frequencies and load capacities. This includes the choice of martial and cross-section areas of different links to reduce the operation and running costs. Therefore, the stress and vibration analysis are conducted to justify the material choice and the robot arm's physical layout. The stress analysis is investigated using FEM and an approximate design method is introduced to select the optimum material. Hence, the analysis done using ANSYS showed that the Aluminum alloy guaranteed high FoS values, acceptable deflection, and high natural frequencies compared with the other alternatives. This is in addition to its relatively low price and lightweight. Furthermore, the results indicated that the links taking diameters from 20 to 70 mm can carry mass-loads ranging from 2 to 16 Kg and would result in a prespecified desired FoS range of (2 to 6). This enabled a simplified robot arm design at any mass-load (Kg) value and cross-section areas. On the other side, the vibration analysis is done using FEM to study the natural frequencies modes and hence introduce recommendations to avoid working at the resonance frequencies. This resulted in a customized robot arm structure that combines Magnesium and Aluminum alloy. The design improves the FoS by 5.9 % compared with an Aluminum Alloy based design and by 56.9 % when compared with Structural Steel based design. Thus, this light design minimizes the operating cost with the same percentages. The natural frequencies are observed to be slightly above 45 Hz and the robot arm avoids operating close to or at the resonance frequencies. In addition to the body structure of the robot arm, the effect of the reducers and motors on the stiffness and vibration of the robot arm is introduced.

Finally, GA is used to optimize the motion of a robot arm where a cost function that penalizes the power consumption of

Table 13 Alternatives using inverse kinematic to reach the end-effector position (0.378, 0.35, 0.28).

Sol. No.	θ_1 (rad)	θ_2 (rad)	θ_3 (rad)	θ_4 (rad)	θ_5 (rad)	θ_6 (rad)
1	0.43777	0.46494	-0.4722	0.08888	5.17e-7	0
2	0.43777	0.484	-0.5	0.16055	0	0
3	0.43388	-0.1238	0.63666	-0.0255	-0.9844	0
4	0.43944	-0.0444	0.56722	-0.2227	0.99722	0
5	0.43777	0.47555	-0.4877	0.12833	0	0
6	0.43777	0.47111	-0.4811	0.11172	0	0
7	0.43777	0.52444	-0.6288	0.54277	0.99055	0
8	0.42333	0.46166	-0.5944	0.82111	0.97416	0

Table 14 Alternatives using inverse kinematic to reach the end-effector position (-0.44, 0.28, 0.31).

Sol. No.	θ_1 (rad)	θ_2 (rad)	θ_3 (rad)	θ_4 (rad)	θ_5 (rad)	θ_6 (rad)
1	0.71944	-0.2896	-0.31289	-0.2733	0.97333	0.86722
2	0.71944	-0.25367	-0.5210	-0.0787	0.90833	0.97216
3	0.80666	0.282167	-0.57939	0.06438	0.16	0.98066
4	0.92666	0.985556	-0.0327	-0.23	0.21	0.11
5	-0.9511	-0.98611	-0.255	-0.1311	0.9644	-0.965
6	0.32444	0.541111	-0.2216	0.02277	-0.0810	-0.5488
7	0.32444	0.821667	-0.99	0.85888	-0.9927	0.99722
8	0.915	0.803333	-0.1105	-0.1322	-0.3577	0.92055
9	-0.9022	-0.84889	0.9	-0.955	-0.9011	0.13555
10	0.82277	-0.86111	0.80633	0.66444	0.98611	0.03555

the robot joints is considered. The presented mechanism identifies the coefficients of a polynomial representing the angular displacement as a function of time. The optimal trajectory (mission) time of 5 Secs was determined based on the minimum consumed power, 94.9 % reduction in power consumption at 5 s relative to 0.5. It is observed also that increasing the rotation angle increases the power only for the very small mission time. This is associated with Robo-Analyzer simulations to find the best alternative solutions for some end-effector positions. Determining the best alternative solutions for some end-effector positions highly minimizes the torque consumption (operating cost).

Data Availability Statement

The datasets generated during and/or analyzed during the current study are available from the corresponding author on reasonable request.

Declaration of Competing Interest

The authors declare that they have no known competing financial interests or personal relationships that could have appeared to influence the work reported in this paper.

Appendix

The matrix coefficients of the equations of motion are given by

$$M_{11} = \frac{1}{3}m_1l_1^2 + m_2l_1^2 + \frac{1}{3}m_2l_2^2 + m_2l_1l_2c_2,$$

$$M_{12} = \frac{1}{3}m_2l_2^2 + \frac{1}{2}m_2l_1l_2c_2$$

$$M_{21} = \frac{1}{3}m_2l_2^2 + \frac{1}{2}m_2l_1l_2c_2, M_{22} = \frac{1}{3}m_2l_2^2$$

$$C_{11} = 0, C_{12} = -\frac{1}{2}m_2l_1l_2S_2, C_{21} = -\frac{1}{2}m_2l_1l_2S_2, C_{22} = 0$$

$$R_{11} = -m_2l_1l_2S_2, R_{12} = 0, R_{21} = z, R_{22} = 0$$

$$G_{11} = \left(\frac{1}{2}m_1 + m_2\right)gl_1c_1 + \frac{1}{2}m_2gl_2c_{12}, G_{22} = \frac{1}{2}m_2gl_2c_1$$

$$C_1 = \cos \theta_1, S_1 = \sin \theta_1, C_2 = \cos \theta_2, S_2 = \sin \theta_2, \\ C_{12} = \cos (\theta_1 + \theta_2), S_{12} = \sin (\theta_1 + \theta_2)$$

References

- [1] J.J. Craig, Introduction to Robotics: Mechanics and Control, third ed., Pearson Prentice Hall, 2005.
- [2] R.M. Murray, Z. Li, S.S. Sastry, A Mathematical Introduction to Robotic Manipulation, CRC Press, 1994.
- [3] M.W. Spong, S. Hutchinson, M. Vidyasagar, Robot Modeling and Control, John Wiley & Sons, 2006.
- [4] B.K. Rout, R.K. Mittal, Tolerance design of robot parameters using Taguchi method, *Mech. Syst. Signal Process.* 20 (8) (2006) 1832–1852.
- [5] W. Li, Z. Li, Y. Liu, L. Ding, J. Wang, H. Gao, Z. Deng, Semi-autonomous bilateral teleoperation of six-wheeled robot on soft terrains, *Mech. Syst. Signal Process.* 133 (2019) 106234.
- [6] R.J. Alattas, S. Patel, T.M. Sobh, Evolutionary modular robotics: Survey and analysis, *J. Intell. Rob. Syst.* 95 (2019) 815–828.
- [7] V. Patidar, R. Tiwari, Survey of robotic arm and parameters, in: Coimbatore (Ed.), International conference on computer communication and informatics (ICCCI), 2016, pp. 1–6.
- [8] S. Saeedvand, M. Jafari, H.S. Aghdasi, J. Baltes, A comprehensive survey on humanoid robot development, *Knowl. Eng. Rev.* 34 (2019) E20.
- [9] T. Fujikawa, K. Hirakawa, S. Okuma, T. Udagawa, S. Nakano, K. Kikuchi, Development of a small flapping robot: Motion analysis during takeoff by numerical simulation and experiment, *Mech. Syst. Signal Process.* 22 (6) (2008) 1304–1315.
- [10] K.J. Kaliński, M. Mazur, Optimal control of 2-wheeled mobile robot at energy performance index, *Mech. Syst. Signal Process.* 70–71 (2016) 373–386.
- [11] L. Zhou, Y. Li, S. Bai, A human-centered design optimization approach for robotic exoskeletons through biomechanical simulation, *Rob. Autonom. Syst.* 91 (2017) 337–347.
- [12] E.J. Van Henten, D.A. Van't Slot, C.W.J. Hol, L.G. Van Willigenburg, Van Willigenburg, Optimal manipulator design for a cucumber harvesting robot, *Comput. Electron. Agricul.* 65 (2) (2009) 247–257.
- [13] J. Fu, F. Gao, Optimal design of a 3-leg 6-DOF parallel manipulator for a specific workspace, *Chin. J. Mech. Eng.* 29 (4) (2016) 659–668.
- [14] S. Singh, E. Singla, Realization of task-based designs involving DH parameters: a modular approach, *Intel. Serv. Robot.* 9 (3) (2016) 289–296.
- [15] G. Zeinoun, R. Sedaghati, F. Aghili, Optimal design parameters of reconfigurable robots with lockable joints, *Trans. Can. Soc. Mech. Eng.* 41 (1) (2017) 23–38.
- [16] A. Csiszar, A combinatorial optimization approach to the Denavit-Hartenberg parameter assignment, *IEEE International Conference on Advanced Intelligent Mechatronics (AIM) 2015* (2015) 1451–1456.
- [17] S.F.P. Saramago, V. Steffen Jr, Optimization of the trajectory planning of robot manipulators taking into account the dynamics of the system, *Mech. Mach. Theory* 33 (7) (1998) 883–894.
- [18] S. Ha, S. Coros, A. Alspach, J. Kim, K. Yamane, Computational co-optimization of design parameters and motion trajectories for robotic systems, *Int. J. Rob. Res.* 37 (13–14) (2018) 1521–1536.
- [19] M. Soysalan, M. Uk, F. Ali Shah, O. Erdogan, Modelling, Control and Simulation of a SCARA PRR-Type Robot Manipulator, *Scientia Iranica* 27 (1) (2020) 330–340.
- [20] J. Ma, Y. Liu, S. Zang, L. Wang, Robot Path Planning Based on Genetic Algorithm Fused with Continuous Bezier Optimization, *Computational Intelligence and Neuroscience* 2020 (2020) 1–10.
- [21] S. Baressi Šegota, N. Andelić, I. Lorencin, M. Saga, Z. Car, Path planning optimization of six-degree-of-freedom robotic manipulators using evolutionary algorithms, *International Journal of Advanced Robotic Systems*, (2020), 17(2), 172988142090807.
- [22] P. Cooper, A. Griffiths, T. Andrzejewski, K. Giannetti, Motion optimisation for improved cycle time and reduced vibration in robotic assembly of electronic components, *AIMS Electronics and Electrical, Engineering* 3 (3) (2019) 274–289.
- [23] J. Amar, K. Nagase, Genetic-algorithm-based global design optimization of tree-type robotic systems involving exponential coordinates, *Mechanical Systems and Signal Processing* 156 (2021) 107461.
- [24] C. Pupačić, G. Constantin, T. Negril, Computer aided engineering of industrial robots, *Proc. Manuf. Syst.* 9 (2) (2014) 87–92.

- [25] S. Sahu, B. Choudhury, Static analysis of a 6-axis industrial robot using finite element analysis, *Int. J. Mech. Eng. Technol. IJMET* 8 (3) (2017).
- [26] N. Francis, K. Urmila, Design and analysis of circular and square arm robot, *Anveshana's Int. J. Res. Eng. Appl. Sci.* 1 (11) (2016).
- [27] C.S.V. Uma Sai Vara Prasad, M. Balaji, Geometric parameters optimization & analysis of packing robot arm using ansys, *Int. J. Adv. Res. Basic Eng. Sci. Technol. (IJARBEST)* 3 (30) (2017) 1–6.
- [28] W. Choong, K. Yeo, Structural design for a 3dof robot lower-arm via computer aided engineering, *Centre Mater. Miner., Universiti Malaysia Sabah* 88999 (2007) 8–18.
- [29] J. Rueda, L. Ángel, Structural analysis of a delta-type parallel industrial robot using flexible dynamic of ansys 11.0, *Industrial Electronics, 2009. IECON'09. 35th Annual Conference of IEEE, IEEE*, 2009, pp. 2247–2252.
- [30] J. Zhou, Z. Yang, S. Chen, Analysis of the harvesting robot arm modal based on cae, *J. Chem. Pharm. Res* 6 (11) (2014) 669–673.
- [31] P.G. Chitte, S.S. Bansode, S.S. Rathod, N.S. Motgi, Structural and vibrational analysis of six axis aristo robot using ANSYS, *IJIRT* 3 (1) (2016) 291–296.
- [32] P. Yao, K. Zhou, Y. Lin, Y. Tang, Light-Weight Topological Optimization for Upper Arm of an Industrial Welding Robot, *Metals* 9 (2019) 1020, <https://doi.org/10.3390/met9091020>.
- [33] K. Mohamed, H. Elgamal, S.A. Kouritem, An experimental validation of a new shape optimization technique for piezoelectric harvesting cantilever beams, *Alexandria Engineering Journal* 60 (1) (2021) 1751–1766.
- [34] S.A. Kouritem, M.M.Y.B. Elshabasy, Tailoring the panel inertial and elastic forces for the flutter and stability characteristics enhancement using copper patches, *Composite Structures* 274 (2021/10/15/ 2021,), <https://doi.org/10.1016/j.compstruct.2021.114311> 114311.
- [35] M.M.Y.B. Elshabasy, S.A. Kouritem, Thickening of optimally selected locations on panels subjected to unyawed flow for substantial delay of the panel flutter, *Alexandria Engineering Journal* 59 (6) (2020/12/01/ 2020,) 5031–5044, <https://doi.org/10.1016/j.aej.2020.09.026>.
- [36] S. A. Kouritem, M. M. Elshabasy, and H. A. El-Gamal, “Optimum Location/Area of PZT Actuators for Flutter Damping Using Norm Feedback Control Gain-Based Iterative Method,” in *The 2015 World Congress on Advances in Structural Engineering and Mechanics (ASEM15), Incheon, South Korea*, 2015.
- [37] S. A. Kouritem, M. M. Elshabasy, and H. A. El-Gamal, “FE Meshing Scheme for Accurate Placement/Area of PZT Actuators for Flutter Damping Using LQR Method,” in *The 2015 World Congress on Advances in Structural Engineering and Mechanics (ASEM15), Incheon, South Korea*, 2015, p. <https://www.researchgate.net/publication>.
- [38] R. Sudarshan, J. Babu, P. Ravinder Reddy, Static Analysis of an Articulated Robot Manipulator Made of Composite Materials using FEA, *International Journal of Engineering Research and Technology* 4 (2011) 373–380.
- [39] G. Shanmugasundar, R. Sivaramakrishnan, S. Meganathan, S. Balasubramani, Structural Optimization of an Five Degrees of Freedom (T-3R-T) Robot Manipulator Using Finite Element Analysis, *Materials Today: Proceedings* 16 (2019) 1325–1332.
- [40] T. Abbott, Why Choose Magnesium?, *Materials Science Forum* (618-619), (2009), (3-6).
- [41] E. Picard, F. Plestan, E. Tahoumi, F. Claveau, S. Caro, Control Strategies for a Cable-Driven Parallel Robot with Varying Payload Information, *Mechatronics* 79 (2021) 102648.
- [42] L. Gharavi, M. Zareinejad, A. Ohadi, Dynamic Finite-Element analysis of a soft bending actuator, *Mechatronics* 81 (2022) 102690.
- [43] L. Srinivas, A. Javed, Topology Optimization of KUKA KR16 Industrial Robot Using Equivalent Static Load Method, 2021 IEEE International IOT, Electronics and Mechatronics Conference (IEMTRONICS).
- [44] S.A. Kouritem, Array of piezoelectric energy harvesters for broadband natural frequency applications, *ICSV27, Annual Congress of International Institute of Acoustics and Vibration (IIAV), Prague*, 11-16 July 2021.
- [45] G. Caprino, A. Langella, Optimization of robotic arms made of composite materials for maximum fundamental frequency, *Composite Structures* (1995) 1–8.
- [46] J. G. Kurebwa, T. Mushiri, Structural Design, Optimization and Analysis of Robotic Arm Via Finite Elements, *Progress in Human Computer Interaction*, (1) 2, 2018.
- [47] A. Lu, J. Xu, H. Liu, Effect of a preload force on anchor system frequency, *Int. J. Min. Sci. Technol.* 23 (1) (2013) 135–138.
- [48] M.A. Chowdhury, M. Ali, M.M. Helali, The effect of natural frequency of the experimental set-up on the friction coefficient, *Ind. Lubr. Tribol.* 62 (2) (2010) 78–82.
- [49] R.N. Jazar, Theory of applied Robotics: Kinematics, Dynamics, and Control, second ed., Springer, New York, USA, 2010.
- [50] J. Parker, A. Khoogar, D.E. Goldberg, Inverse kinematics of redundant robots using genetic algorithms, *IEEE Int. Conf. Robot. Autom.* 1 (1989) (271-176).
- [51] M.M.Y.B. Elshabasy, K.T. Mohamed, A.A. Ata, Power optimization of planar redundant manipulator moving along constrained-end trajectory using hybrid techniques, *Alexandria Engineering Journal* 56 (2017) 439–447.
- [52] K. Mohamed, H. Elgamal, A. Elsharkawy, Dynamic analysis with optimum trajectory planning of multiple degree-of-freedom surgical micro-robot, *Alexandria Engineering Journal* 57 (2018) 4103–4112.
- [53] Y. Davidor, Genetic algorithms and robotics: a heuristic strategy for optimization, in: *World Scientific Series in Robotics and Automated Systems*, vol. 1, Teaneck, NJ, USA, 1991.
- [54] J. Denavit, Jacques, R. S. Hartenberg, A kinematic notation for lower-pair mechanisms based on matrics. *Transactions on ASME Journal of Applied Mechanics*, (1955), 23, 215–221.
- [55] K. Raza, T.A. Khan, N. Abbas, Kinematic analysis and geometrical improvement of an industrial robotic arm, *Journal of King Saud University –, Engineering Sciences* 30 (2018) 218–223.